Preparation, characterization and testing of model catalysts for CO oxidation and CO_2 hydrogenation

Stefano Albertin

LUND UNIVERSITY

Author:
Stefano Albertin

Supervisors:
Uta Hejral
Johan Gustafson

A Thesis Submitted for the Degree of Master of Science
Project Duration: 4 Months

Division of Synchrotron Radiation Research
Department of Physics
Faculty of Science

June 2nd, 2017

Preparation, characterization and testing of model catalysts for CO oxidation and CO_2 hydrogenation

STEFANO ALBERTIN | DEPARTMENT OF PHYSICS | LUND UNIVERSITY

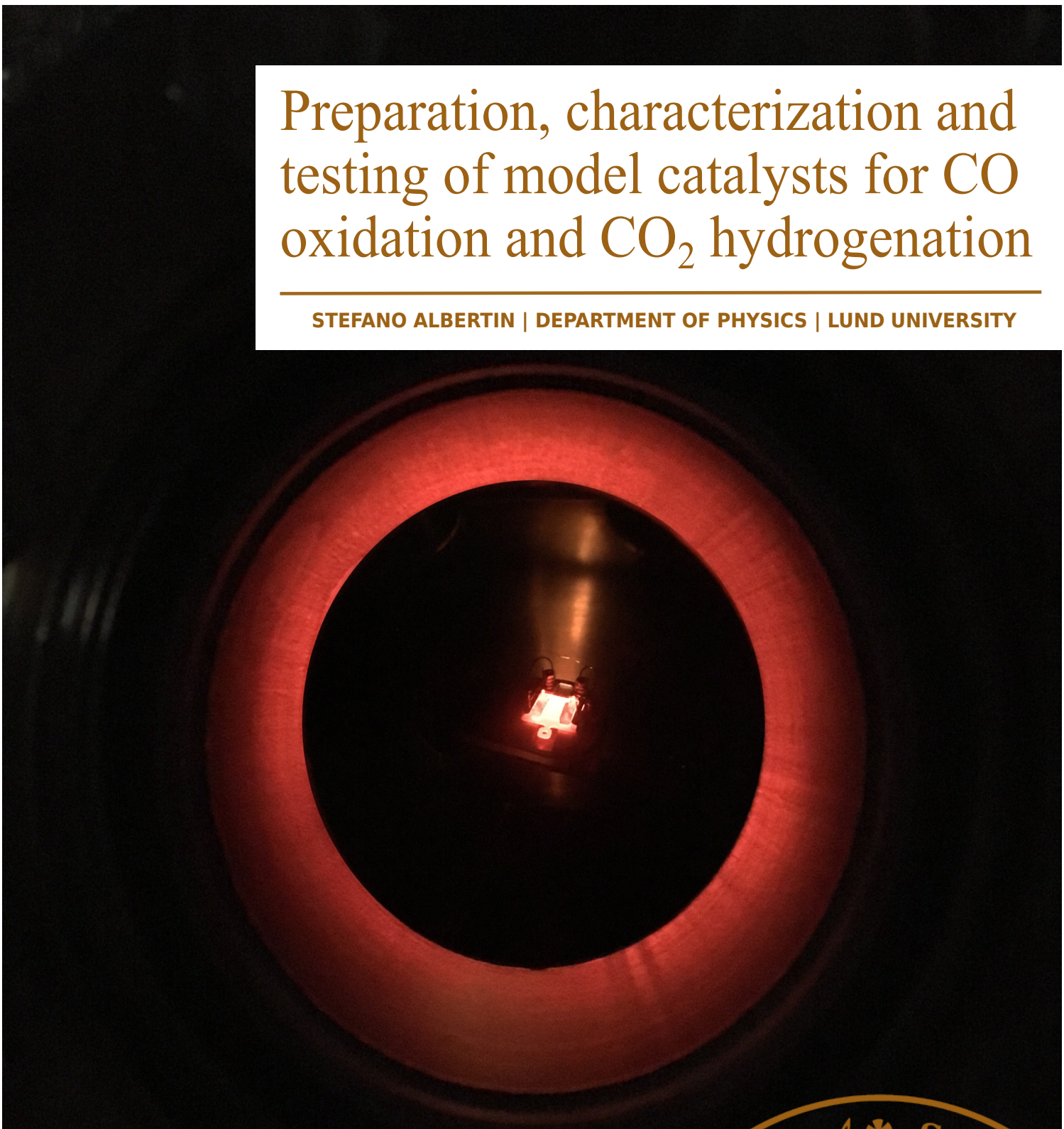

Div. of Synchrotron Radiation Research
Department of Physics
Faculty of Science
Lund University

June 2017

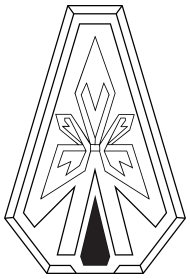

"Certainty of death...
Small chance of success...
What are we waiting for?"
-Gimli, son of Gloin-

Contents

Popular Abstract

Alcohol from CO_2, without the need of systembolaget

Nowadays, the release of CO_2 in atmosphere is of great concern due to its nature of greenhouse gas, and connection to global warming. Of growing importance is also the so-called carbon economy, stricly linked to CO_2 release: that is the net amount between carbon emitted and sequestrated. In this scenario then, bringing to a theoretical zero the effect of a certain amount of CO_2 once sequestrated, for instance "recycling" it. If we want to pursue this "recycling" path then, due to the laws of physics, we have to note that CO_2 is one of the most stable forms of carbon in nature and to yield an economically feasible process we have to *catalyse* the reaction. Where, the products more likely to be obtained through this reaction, are so-called C1 and maybe C2 carbon compounds: chemicals with one or two carbon atoms, and among them two of the most desirables, alcohols like methanol -CH_3OH- or ethanol -C_2H_5OH-.

From a previews joint research between Lund University and the Chalmers Competence Centre for Catalysis, promising results have been brought up about the chance to obtain valuable chemical by CO_2 catalysis. Specifically, my work deals with the study of CO oxidation as a prototypical reaction for the CO_2 hydrogenation on model catalyst. This, in order to understand the physical mechanism behind it, and to eventually use it in multiple contexts.

The original catalyst, consisted of nano and micro particle of Rhodium of not well definite size, distributed on a 3D "sponge-like" oxide. However, since this system is too complex to be studied in detail, a "model catalyst method" have to be applied. This consists in designing, fabricating and characterising a simpler model of our desired catalyst in order to ease its analysis. At the same time, while doing this, we try to be as close as possible to the original system in order to gain representative results. To do this, we deposited two samples of Rhodium nanoparticles on flat oxide substrate, and a third with the add of Cerium Oxide on top of it. Then we analysed the surface with nanometric resolution in order to understand the samples characteristics, and test the catalytic activity against a "traditional" catalyst, in order to compare

their behaviours.

While for the "traditional" catalyst we confirmed well known characteristics in our sample we observedan interesting behaviour, not yet observed in the literature. Further studies are needed to gain a complete picture of the system: from CO oxidation on all the samples, to CO_2 hydrogenation itself. But previous studies, and the new unexpected results, foster a cautious optimism. Perhaps, in the future, we will be able to do have catalyse alcohol from thin air!

Abstract

A joint research between Lund University and Chalmers Competence Centre for Catalysis have shown promising results for a Rh-based catalyst for CO_2 hydrogenation catalytic applications. The original catalyst consisted of a dispersion of nanoparticles onto a porous 3D oxide network. To gain a deeper understanding of the catalyst, a surface science study is necessary, but it is impossible to perform on the original system, because of its complexity. For this reason, in this work a model catalyst approach has been tested along with the use of CO oxidation as a prototypical catalytic reaction.

A total of three model catalyst samples was prepared via physical vapour deposition: two consisting of Rh nanoparticles on MgO(001) and a third that in addition have CeO_x deposited on Rh particles. The characterisation was done by AFM and SEM microscopies, and showed for all three samples a comparable particle growth with particles equally distributed over the substrate surface with heights and diameters of 3 nm and 20 nm, respectively. Moreover, the presence of a complex system of micro- and nano-particle was noted on one of the Rh/MgO samples, showing the effect on deposition of different substrate preparation parameters. After the characterisation, we proceeded with the catalytic activity tests.

The tests for CO oxidation were performed on two samples: one Rh/MgO sample and one Pd/Al_2O_3 powder catalyst, using a catalysis flow-reactor specifically implemented for this work. The tests on Pd/Al_2O_3 showed a high catalytic activity with activity oscillations under conditions characterized by oxygen overstoichiometry. These oscillations, as previously reported in the literature, are explained by means of a non-equilibrium oxidation phenomenon periodically shutting off the activity of the catalyst surface.

The Rh/MgO on the other hand, showed a generally lower catalytic activity and higher activation energies. Most interesting though, was the presence of an unexpected oscillatory behaviour of the catalytic activity under conditions of CO overstoichiometry, a behaviour not yet reported in the literature. In this scenario, our hypothesis of reaction mechanism for this oscillatory behaviour, involves a non-equilibrium mass transfer limited phenomenon, in which the cyclic depletion of the limiting reactant, O_2, is responsible for generating the oscillations.

Further tests will be needed to confirm the observed mechanism, using the

remaining two samples during CO oxidation, and to eventually test possible contributions from the CeO_x to the reaction. Furthermore, catalytic reactivity tests on the same three samples for the CO_2 hydrogenation have already been scheduled in the meantime.

List of Acronyms

Acronim	Definition
AES	Auger Electron Spectroscopy
AFM	Atomin Force Microscopy
UHV	Ultra High Vacuum
LEED	Low Energy Electron Diffraction
SEM	Scaning Electron Microscope
TWC	Three Way Catalyst
CMA	Cylindrical Mirror Analyser
NPs	Nano-Particles
MPs	Micro-Particles
QMS	Quadrupol Mass Analyser
E_a	Activation Energy
RGA	Residual Gas Analysis
MTL	Mass Transfer Limit

Chapter 1

Introduction

Global warming has been known for decades now [1] and for almost the same amount of time we have been also aware that this is mainly caused by the introduction in the atmosphere of so-called greenhouse gasses: of which CO and CO_2 are two of the major components [2]. At the same time, both constitute also two of the most ubiquitous by-products of major industries, manufacturing process and human activities in general: being recognised nowadays as one of the major environment issues. For these reasons, further than the reduction of production of these chemicals at the source, a multilateral approach is advisable.

One of the possible approaches then is to "recycle" these gasses, in order to use them to produce valuable goods, at the same time providing an economically feasible carbon sequestration method. In this scenario, is also easy to verify how a number of industries use a variety of so-called C1 and C2 chemical compounds in their production processes [3]. The same products that are more likely to be obtained by catalysis of C1 chemicals such as CO and CO_2[4, 5, 6].

Due to the laws of kinetics though, these two carbon compounds are at STP -standard temperature and pressure- conditions stable for an indefinite time: so that the only way to obtain a chemical reaction is to modify the conditions in which this take place. The *par-excellence* method, employed for almost a century now [7], to solve this issue is catalysis.

In this context, a joint research of Lund University and Chalmers Competence Centre for Catalysis, highlighted some promising results for CO_2 hydrogenation, at relatively low temperature and ambient pressure, for Rh-based catalysts. Since the possible benefits, a further investigation has been believed needed. Specifically, in this work will present the preparation, and testing for CO oxidation, of Rh/MgO and CeO_x/Rh/MgO samples, as model catalysts for CO_2 hydrogenation.

Using commercial available slabs of MgO(001) 10x5x1 mm^3 as substrate, we prepared three different samples, and characterised each of them with both Atomic Force (AFM) and Scanning Electron Microscopies (SEM). The first sample was prepared by Ar^+ sputtering at 500 eV, and O_2 annealed. The Rh deposition was done on heated sample and via Physical Vapour Deposition (PVD): obtaining a homogeneous nanoparticle (NPs) distribution of around 20 nm in diameter and 3 nm in height. The second sample, sputtered at higher energy of 1,5 keV, presented Ar embedding during Auger Spectroscopy (AES) analysis. The damage left from the Ar to the surface has lead to the formation of a coexisting system of nano- and micro- particles on the sample surface. The microparticles (MPs), accounting for an 8% coverage, present a 1,5 μm diameter and 60 nm height, while the NPs diameter and height is consistent with the results on the previous sample. The third sample, prepared with the sample recipe from the first sample, have undergone a subsequent reactive PVD deposition of CeO_x.

The CO oxidation tests were conducted with a custom gas-system implemented specifically for this work. The catalytic tests were conducted on one sample of Rh/MgO, and a reference sample of powder catalyst. This, consisting in Pd on Al_2O_3 was in form of pellet. The test were conducted at 4 different gas-ratio compositions, employing CO and O_2 as reactants and Ar as carrier gas. A complete temperature cycle 25°C to 500°C and back was performed for each sample and for each gas-ratio. The reference sample Pd/Al_2O_3, as expected, showed during all the tests an high catalytic activity with activation energies decreasing on increasing O_2 concentrations. Furthermore, as already reported in literature, an oscillatory behaviour in the catalytic activity was found in oxidising atmospheres. The Rh/MgO sample showed a similar behaviour in catalytic activity, even if lower compared to Pd/Al_2O_3. Major difference, and not yet observed in literature, was the absence of oscillations for O_2-rich atmospheres, but instead, an oscillatory behaviour in CO-rich conditions.

This new catalytic behaviour, observed only in nearly stoichiometric condition, has been proposed to be due to a non-equilibrium distribution of oxygen on the catalyst surface during the reaction. Contrary to the mechanism involved in the Pd/Al_2O_3 O_2-rich oscillation though, this supposed mechanism do not involve any surface reconstruction, but a mass transfer limited reaction of the limiting reactant, O_2, to the catalyst surface.

Further tests will be needed to confirm the observed mechanism, characterised the other to samples and to eventually observe any possible contribution from the CeO_x to the reaction. Furthermore, a complete catalytic reactivity tests on the samples for the CO_2 hydrogenation has already being scheduled in the short term.

Thesis Outline

For what concern the layout of the following work, it will be organised in two main conceptual blocks following a path that from generic will get a more and more detailed with the ongoing chapters and sections.

In particular the first conceptual block will be constituted of Chapter 2 and 3 that will deal with the Theoretical Background needed for this work's analysis, and the Methods and procedures' details used in developing the work. The second block, instead, will present and analyse in Chapter 4 and summarise in Chapter 5 the results obtained. Finally, in Chapter 6, we will see an outlook for further developments of this thesis work, to get a broad picture of the possible near future.

Chapter 2

Theoretical Background

In this chapter will be treated the theoretical background and great part of the terminology that will be used in this work. The subsections are divided by conceptual area and more or less listed in specificity order: from the most generic to the more detailed one.

In particular, in Section 2.1 will be treated the concept behind the catalytic process and, in particular, a typical oscillatory behaviour in a catalytic activity that will become relevant during our analysis in Section 4.3. In Section 2.2 instead a will be taken a closer look to the catalyst itself: its morphology and the specific composition used for this work. Finally, in Section 2.3, we will briefly discuss the meaning of CO oxidation, and the role of a model catalyst.

2.1 Concept of catalysis

> *"The body effecting the changes does not take part in the reaction and remains unaltered through the reaction. This unknown body acts by means of an internal force, whose nature is unknown to us. This new force, up till now unknown, is common to organic and inorganic nature."*
>
> *Berzelius , 1835 [7]*

Catalysis constitutes an umbrella term for chemical reactions taking place with the intervention of a third component besides reactant and product. The catalysts are as *"A substance that increases the rate of a chemical reaction without itself undergoing any permanent chemical change"* [8, 7]. Which gives us an introduction to the kinetics influence of a catalyst on a chemical reaction.

Catalysts can be classified into three main relative broad categories. Based on their specific nature and the relative phase to the reactants: Homogeneous-, Bio- and Heterogeneous- catalysts [9, 8, 10]. In case, both catalyst and reactants, share the same phase, the reaction is classified as "homogeneous": examples can be found in polymer chemistry for instance [11]. Bio-catalysis usually take place in biological environment and thanks to complex protein catalysts. As the name suggest, almost the entire biological activity as we now it, falls under this definition. When catalyst and reactants are in different phases, the reaction will be labelled as "heterogeneous": in particular, this work will study a gas-solid heterogeneous system.

Known and heavily used for almost a century, catalysis is now of primary importance in manufacturing processes carried out across multiple industries: from food processing to petrochemical industries, from pharmaceutical to electronics; this class of chemical reactions is responsible for a business accounting for billions of dollars per year [9, 8].We can state that catalysis, nowadays, represents the very foundation on which the industrialised world is based upon, which triggers the need for a deeper understanding of its mechanisms, in order to better exploit and design these components.

Based on the aforementioned, it becomes clear that knowledge about the correlation between catalyst structure and catalytic activity is of crucial importance since, especially in the case of heterogeneous processes, the intervention of Surface Science at the interface between the two phases become essential to unveil the mechanisms behind the reaction itself: precisely here is where the physics, and in particular the Synchrotron Radiation Division, come into play.

2.1.1 Chemistry and Physics of catalysis

Driven both by thermodynamic and kinetic factors, a general chemical reaction can be pictured like in Fig. 2.1, using reaction coordinate as standard representation. The reaction will take place, with the chemicals interacting with the catalysts' surface, in three main steps: absorption, reaction and desorption

Considering the example in Fig. 2.1 we can notice how, between reactants and products, several steps can occur, with multiple metastable intermediate states in between. Moreover, considering every partial reaction, each one will present its own specific energy barrier, also called Activation Energy -E_a-. This E_a, briefly introduced in Eq. 2.1, constitutes the initial energetic requirements for the system to break the bonds in between the atoms, in order to form new ones. The catalyst purpose is then to lower these activation energies in order to accelerate the reaction to its natural thermodynamic

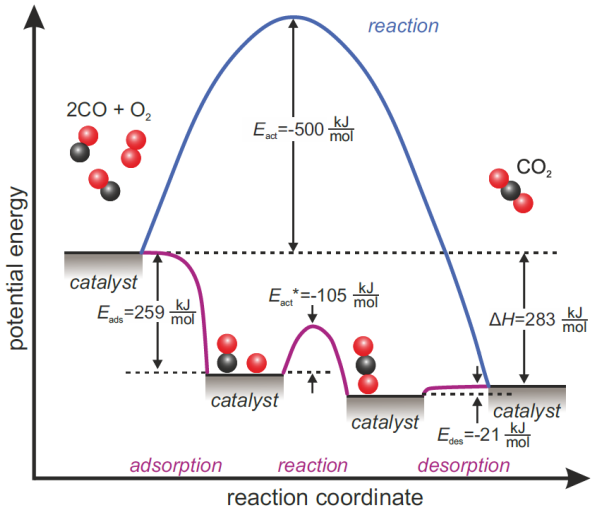

Figure 2.1: *Example of energy diagram for CO oxydation on Pt(111). In blue the un-catalysed path withe its E_a, in purple the catalysed multi-step path. As can be seen the enthalpy , which defines the thermodynamic equilibrium for the reaction, is equal for both the paths.* [1]

equilibrium (Fig. 2.1). This can be done creating partial or temporary bonds between reactants and the catalyst: stabilising the reaction intermediate and extending its lifetime, lowering then the kinetics requirements on the system, for a successful reaction.

$$A + B \underset{k_r}{\overset{k_f}{\rightleftharpoons}} C; \quad K = \frac{k_f}{k_r} = Ae^{-\frac{E_a}{k_b T}} \tag{2.1}$$

Where in Eq. 2.1 A,B and C are the concentration of the reactants. In a chemical reaction in which both forward and reverse reactions are possible, k_f and k_r are their rate constants; with K being the equilibrium constant. Where K can be also defined by thermodynamics factors as the activation energy E_a, Boltzmann constant k_b, temperature T and a prefactor A.

The problem can be also approached within a kinetic-theory-of-gasses approximation: since the reaction takes place between many particles, these have to have a physical interaction to participate in the reaction. The more complex the reaction, or shorter lived the intermediates, the lower the statistical chance for this "positive match" to happen for a given time unit. In order to maximise the chance of this "positive match" we can either use

[1] picture taken from *Operando Characterization of Supported Alloy Nanoparticles during Catalytic CO Oxidation by Surface Sensitive X-Ray Diffraction*, Uta Hejral, Hamburg, 2015

a catalyst, or heat the system. The catalyst will either lower the number of molecules involved in each single step, providing more intermediate steps, or lengthen the life-time of active states [9, 8, 10]. The heating will instead increase the average speed of the molecules, providing more interactions per time-unit.

Instead, looking at the "catalytic problem" from the interaction-energy point of view, we can notice how the interaction between reactants, reaction products and the catalyst surface influences the probability of a reaction: this constitutes the core of the *Sabatier principle*. In fact for higher absorption energies, so called chemisorption, the system will favour enormously the adsorption step but not the desorption. For weaker interaction energies, named physisorption, we will have a good balance between energy steps and then a good catalysis; but for too weak interaction no absorption will take place, so that there is no time for the chemical reaction to occur.

Since the catalytic reaction takes place at the catalyst surface, its characteristics are of capital importance. The reaction, in fact, will be influenced by a number of different factors, depending on both substrate and reactor environment:

- the substrate composition and morphology
- individual-gas partial-pressure ratio
- total pressure
- temperature
- match between electronic structure of substrate and reactants

These are all factors that deeply affect the reactivity and mechanisms chosen from the reaction. All of these will be dealt with, one by one, in the following sections: morphology of substrate, and energy interaction in Section 2.2.2 , pressure and temperature in Section 2.3.

In the next section, we will describe the reaction mechanisms that have been found in heterogeneous catalysis.

2.1.2 Mechanims and reactivity

The three main mechanisms that have been identified during the years to be responsible for catalytic effects on the surface of a heterogeneous catalyst are: Langmuir-Hinshelwood, Eley-Rideal, Mars-van-Krevelen; each of them will be described in the following. For further insight see [8, 10].

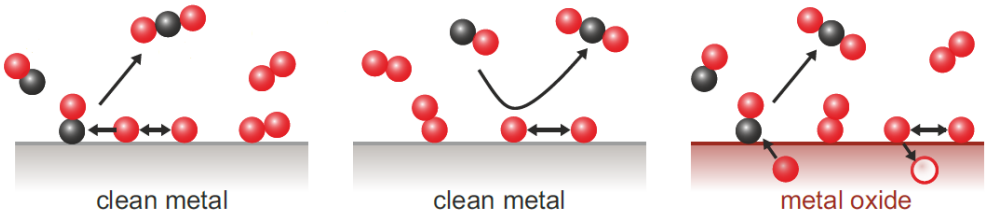

Figure 2.2: *Three main reaction mechanisms with shown molecularity. From Left to Right: Langmuir-Hinshelwood, Eley-Rideal and Mars-van-Krevelen* [2]

In the Langmuir-Hinshelwood mechanism both of the components of the reaction will be adsorbed on the surface, constituting a three step reaction, as can be seen from Fig. 2.2 *left*. So that the reaction will be $A + sub \rightarrow A_{ads}$, $B + sub \rightarrow B_{ads}$ and $A_{ads} + B_{ads} \rightarrow C$.

The Eley-Rideal model is based on the reaction between a physisorbed molecule and a free reactant, so that the reaction will be $A + sub \rightarrow A_{ads}$ and $A_{ads} + B \rightarrow C$. As can be seen in Fig. 2.2 *centre*, this is composed of basically two main steps: the adsorption of A and the reaction between A_{ads} with B with consequent desorption of C.

The Mars-van-Krevelen mechanism will have a different molecularity: until now an implicit assumption was that the substrate is just a platform of weak physical interaction and interplay within two chemicals. In this mechanism, on the contrary, the substrate and in particular its oxide, constitute an active part of the reaction. The result is illustrated in Fig. 2.2 *right* with the equation: $A + Ox \rightarrow C + Red\ O_2 + 2Red \rightarrow 2Ox$ where Ox and Red represent the oxide and reduced site respectively on the catalyst surface.

2.1.3 Oscillations

A topic worth mentioning in a separate section is the oscillatory behaviour in the catalytic activity that is sometimes found on the brink of a mass transfer limit (MTL) for many catalysts. The MTL represents the upper limit in catalytic activity and is defined as the interval of thermodynamic variables in which the Turn-Over Frequency (TOF) of the reaction, which can be identified as the speed of the catalytic reaction, is limited by the amount of raw reactants that can be transferred to the catalyst surface [12, 13], rather then by the activity of the catalytic site itself. The oscillations then derive

[2]picture taken from *Operando Characterization of Supported Alloy Nanoparticles during Catalytic CO Oxidation by Surface Sensitive X-Ray Diffraction*, Uta Hejral, Hamburg, 2015

from a metastable equilibrium in the boundary conditions on the catalyst surface.

This boundary conditions can arise from a multitude of different thermodynamic variables, and have numerous effects on the system. For practical purposes then, we will limit the discussion to what will be of use in this work, specifically treated under section 4.3.

The first, and simpler non-equilibrium boundary-condition, is the uneven distribution of gasses between the first neighbouring of the catalyst and the rest of the reactor environment, where all other surface processes are neglected. This difference in gas concentrations, mainly due to limited diffusion length in gasses [14], can in turn alter the catalyst behaviour with respect to the local gas-composition. In this scenario, a metastable equilibrium between "the first neighbourhood" and the rest of the reactor gas concentrations is found; so that the catalytic activity and gas-composition influence each other in, if not perturbed, close-loop cycles.

The second type of non-equilibrium phenomenon, that can generate oscillations in the catalytic activity, is similar to the previous one but taking into account also reconstruction phenomena from the catalysts' surface itself. Specifically, if an oxide phase is grown on the top of the catalyst, the equilibrium that at first was at two components now present three distinct variables: reactor-environment, first-shell-gas and oxide phase. Up to now, this kind of oscillatory behaviour has been registered only on O_2 rich atmospheres, and has been shown to be due to the O_2 potential. As discussed in previous sections, a thin shell of oxide layer on the metal surface has sometimes been observed more catalytically active, compared to pure metallic phase, and so the reason why in slightly oxidizing atmospheres the catalysts may have a better TOF. Nonetheless, an extended exposure to high oxygen pressures tend to grow a thick oxide shell that ultimately deactivate the NPs. In this condition, though, the CO will gradually reduce the oxide on top, reducing its thickness, and giving rise to the oscillatory behaviour in catalytic activity observed at the mass spectrometer.

2.2 Catalyst

As already mentioned catalysis' industrial role, nowadays worth billion of dollars [9, 8], has become important in the beginning of the 20^{th} century [7]: the need for catalysts peaked with the advent of ammonia synthesis and petrochemical industry for military uses in both the World Wars. The use of this technology, though, has spiked since around the 1970 thanks to the adoption in the automotive industry of the so-called *Three Way*

Catalyst (TWC) for treating the car exhaust [7]. These types of catalysts are the foundation of an entire family in also our model catalyst belongs to. These were, and still are, composed of a support on which the "active components"[3]are dispersed. The substrate, most of the cases made of porous oxide -zeolites-, are the convenient and resilient base on which to deposit the more delicate and expensive "active component". This is almost exclusively composed of a fine dispersion, usually *nanoparticles* (NPs), of a variety of noble and transition metals or rare earth elements [15, 16, 17, 18, 19, 12, 13, 5, 4, 20, 6, 21, 22, 23, 24]. Characteristics of which have been proven, during the years, to have an high *activity* and *selectivity* in these kind of gas reactions.

Noteworthy is the also the fact that, on "real catalysts" industrial scale, a mixture of multiple metals in a dispersion of not precise dimension is generally used on a porous substrate. This is done in order to provide reliable and efficient catalysis on multiple reactions, and at the same time saving costs increasing the general efficiency.

2.2.1 Model catalyst

As aforementioned, the system studied during this work belong to the TWC catalysts family, particularly its, so called, "model catalyst". Model catalyst, in fact, is the definition given to a similar system compared to the original one, but where all its characteristics are strictly defined.

This is required because the complex system that is the "real catalyst" would be impossible to study in detail: so a "model" have to be recreated and tested. In our specific case, a deposition via PVD of a well-ordered NPs bed of a single metal, Rh, with a precise and uniform particle size. This will limit the degrees of freedom of the system allowing a good theoretical study of the system.

A further issue worth mentioning while dealing with a model catalyst is the so-called "material and pressure gap" problem. This is related to the relative distance between environmental conditions of studied model catalyst and real-world applications. In fact, further away is the system studied from its application conditions, worse will be its understanding of the mechanism itself. As the name implies, the two major issues are related to the material gap, addressed in the previous paragraph, and the pressure in which the experiment is performed. In fact, seldom, in order to be able to perform specific analysis, the system have to be studied at low pressures.

[3]even if the term *active component* is fundamentally wrong for what we want to show, in this broader overview seemed appropriate to over-simplify the system. A more exact definition and detailed treatment will be right in the next Section 2.2.2

Key point of this work will be the minimization of these two gaps. In fact, the material gap will be addressed using a composition for our model almost identical to the original. Whether the pressure gap will be addressed working at 800 mbar of total pressure, in contrast with many other surface science studies conducted at 7-10 mbar.

Then, to finally understand the characteristic of a heterogeneous catalyst, we must analyse and understand more in depth every aspect of its morphology, and even more important: the physical behaviour that this brings about.

2.2.2 Morphology

The morphology of the catalyst represents one of the key features that will drive the chemical reaction. In the following section we will describe the general composition of the system that will constitute our case of study, whether a specific description of the system analysed in the following section will be given in Section 2.2.3.

The elements that we are going to analyse will be: the substrate/oxide and the metal on top.

In this description a number of surface science concepts like: epitaxial growth, lattice mismatch, crystal defects and so on; will be given for granted. This because, even though of relevance for this work, they do not constitute the main goal of this work. For more details a number of reference are available, for instance [9, 8, 10]

Metal

The metal constitutes the principal component in the catalytic mix. Its efficiency, also referred as TOF , will be determined through a good energetic balance between adsorption and desorption energies as introduced in 2.1.1 with the concept of *Sabtier Principle*. As also discussed before, most of the chosen elements for catalyst are either transition metals or rare-earth elements, and this is actually the case because of their peculiar electronic nature. The interaction between metal and reactants is possible due to a partial overlap of electronic bands of the two: in particular this overlap has to be spatially and energetic feasible. The elements that show catalytic activity use to have a so-called partially filled d-band. This because in its turn, the d-band shows to have a sufficiently extended volume and a good match to the energy of the molecular orbital of the reactants. Ultimately, due to these required characteristics, only a few metals can be chosen as catalysts [23, 21].

Another important variable in reactants-metal interaction will be, due to geometric/energetic considerations, the relative morphologies. For instance,

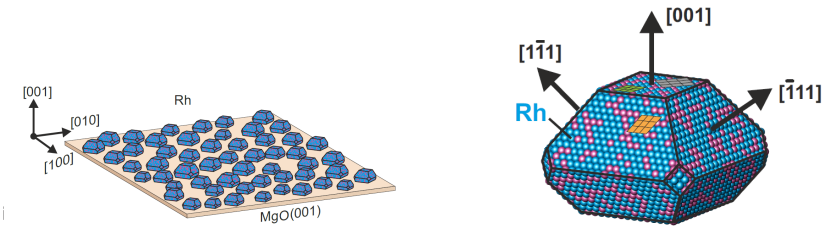

(a) Rh on MgO(001) (b) Rh facets

Figure 2.3: *Example of Rh NPs on MgO(001) on picture (a), with a close-up image of the NPs orientation and relative facets on picture (b)* [4]

the relative lattice parameter of the substrate is of relevance only if compared to the one of the metal to deposit. Due to the anisotropic surface energy γ_i between different facets, and with the consequent application of the *Wulff-Kaishew theorem* 2.2 and the *Dupré equation* 2.3: the shape of the supported NPs will be determined in great part from the adhesion energy with the substrate, as shown in Fig. 2.4. In this E_{adh}, the γ_{int} will be uniquely constituted by the couple metal-oxide: and in particular from their electronic interaction, that will be greatly influenced by the relative crystal geometries and lattice parameters.

$$\frac{\Delta h}{h_i} = \frac{E_{adh}}{\gamma_i} \tag{2.2}$$

$$E_{adh} = \gamma_{met} + \gamma_{ox} - \gamma_{int} \tag{2.3}$$

Where in *Wulff-Kaishew theorem* 2.2: Δh represents the truncation height of the NPs at the interface while h_i is the relative high of a crystal facet to the NPs center [12, 13]. We will be then able to stabilize huge varieties of NPs geometries just with this parameter, as shown if Fig. 2.4 *(c)*

Specifically, this is the case because of the energetic anisotropicity of crystal facets and high contribution of γ_i to the total ΔG of the NPs, as already discussed before. The equilibrium shapes then will vary depending on the systems' conditions. Furthermore, the metal morphology saw in Fig. 2.3 will be deeply affected by environmental variations: temperature, pressure and gas composition. This will ultimately determine a huge variety of "independent systems", based on thermodynamic conditions.

Finally, for the metals, we can then identify multiple shape-shifting processes: as surface reconstructions phenomena, or so-called Ostwald and Smoluchowski ripening processes [9, 23]. All of them will gain more and more

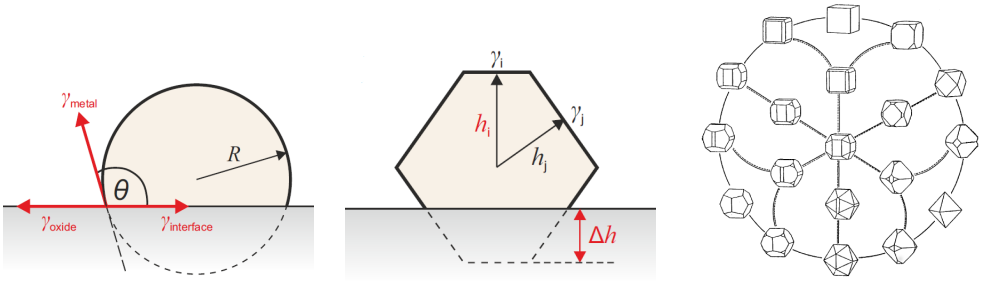

(a) Isotropic Wulff-Kaishew (b) Unisotropic Wulff-Kaishew (c) Piryte crystals' shapes

Figure 2.4: *Wulff-Kaishew construction for (a) isotropic material and (b) a crystal structure. Where γ_i, γ_{met}, γ_{ox} and γ_{int} represent various surface energies. Δh and h represent the relative heights and truncation hight and θ the contact angle between particle and substrate. In (c) instead, a overview of possible shape shift with various ratios between facets; in this case they are the natural shapes of pyrite crystals* [5]

importance when compared to the thermodynamic history of the system, and their relation to the catalytic activity.

For all the aforementioned reasons, identified in Material Science also as material- and pressure- gap problems, we will then need to study the system of interest in a condition the closest to the final geometry and environmental conditions as possible.

Substrate/Oxide

The relevance of the characteristics of the substrate is mainly due to its relative physic-chemical characteristics to the metal of which will constitute the bed of. Analysing its important characteristics we can identify: presence of surface defects, the oxide activity and relative lattice parameter.

One of the most important factors to take into account will be the "quality" of the surface itself: this derives from the fact that an atomically flat and perfect surface is not achievable. From this consideration, even assuming to discard the grossest defects, such as 3D screw dislocation and similar, we still

[4]picture taken from *Operando Characterization of Supported Alloy Nanoparticles during Catalytic CO Oxidation by Surface Sensitive X-Ray Diffraction*, Uta Hejral, Hamburg, 2015

[5]picture *(c)* taken from *Morphology of supported nanoparticles*, Claude R. Henry, Progress in Surface Science 80 (2005) 92–116; pictures *(a)* and *(b)* taken from *Operando Characterization of Supported Alloy Nanoparticles during Catalytic CO Oxidation by Surface Sensitive X-Ray Diffraction*, Uta Hejral, Hamburg, 2015

have to consider so-called 2D, and most commonly, 1D defects. In the family of 2D defects there are kinks, steps and higher index facets. Ubiquitous, are instead the 1D defects such as adatoms, vacancies and substitutional defects from foreign atoms. All these types of defects will affect locally the growth of the particles: in particular these defects will serve as preferential adsorption sites due to the presence low coordination sites[12, 13].

The oxide influence once considered of secondary importance, is now taken more and more into consideration when designing new catalysts [25, 13]. To note that in this case, with the word "Oxide", we intend all kind of possible oxides that have a surface contribution: from the substrate, to the possible oxidated surface of NPs, to the introduction of yet another type of non-native oxide phase: where in particular in this work will also be presented a sample in which will be added some CeO_x [26, 27, 28, 5, 4, 20].

The influence of the oxide can be roughly classified under two different points of view: the first one is the oxygen activity in reference to the Mars-van-Klevelen reaction mechanism presented on Section 2.1.2. The second one, instead, has more to do with the electronic interaction between its native electronic structure and the catalytically active states in the metal belonging to the NPs with a similar approach to Density Functional Theory (DFT) approached for the previous section. This interaction gives also rise, especially at the interface, to so-called "mixed states": which contribution extent has not yet been fully understood [12, 13, 29, 20].

For these reasons, as clear from literature, the prominent choice is of oxide of Al, Ce or Mg and similar metals. They constitute a cheap, reliable and well-studied base on which deposit. Moreover their contribution has been studied and classified: this gives us a further degree of freedom to optimize our catalysts' system.

2.2.3 Specificity of Rh/MgO(001) and CeO_x/Rh/MgO(001)

While in the previous section we treated the general considerations around the choice of a TWC-type of catalyst, in this short section we will focus on the specific combination used in this work.

MgO(001) represent a well-studied surface as model catalyst [17] and across industry and academia has shown its reliability as other many oxides. Its surface, non-polar and with a square lattice with a lattice constant of 4,2 Å, has been proven to favour an epitaxial growth of Rh in orientation Rh(001), given the Rh lattice constant of 3.8 Å.

For what concern the metal, Rh was chosen its renowned catalytic activity linked to its electronic structure discussed in 2.2.2. Well known catalyst, can constitute an interesting case of study and with plenty of comparative

articles can advantage a more complete understanding of the mechanisms [15, 17, 5, 6, 25, 30, 14, 31, 23, 32].

CeO_x has been previously found particularly active as "oxygen donor" on catalyst surface due to its high oxidations numbers (Ce^{3+} and Ce^{4+}). Moreover, in thin films has been observed a high concentration of O vacancies on the surface, particularly active site since the low coordination atoms in the fist neighborhood The presence of CeO_x has also been found particularly active in forming mixed surface states thanks to corrugation and charge transfer phenomena: that results of particular interest in studying different influences on catalytic activity. Finally, it is observed a good epitaxial growth despite the Rh/CeO_x lattice mismatch, thanks to super-cell match. [27, 28]

2.3 CO oxidation as catalytic prototypical reaction

As already mentioned in the introduction, nowadays CO_2 is one of the major threats to society due to its effect on global warming [2, 1]. For this reason an environmentally and economically viable solution to the problem is the synthesis of valuable C1 and C2 through CO_2 hydrogenation.

First of all though, another and more reliable catalysis should be tested in order to gain further insight into the catalyst mechanisms: CO oxidation. In fact, as mentioned above, the CO oxidation process constitute the very foundation of heterogeneous gas catalysis. Studied for decades, and with solid theoretical foundation, constitute the cornerstone for catalytic activity analysis [21]. Moreover, during long years, this process has been studied in multiple conditions, exploiting almost completely the hypersurface of the possible experimental results: it then constitutes the ultimate gold standard.

For these reasons we will proceed to study this important process: in order to place our new system in a very well known frame of reference.

Chapter 3

Methods

In this chapter, we will deal with the techniques and methods used throughout this work, for preparation and characterization of the model catalyst sample for testing their catalytic activity during CO oxidation. The chapter will be divided mainly into three sections following the conceptual development of the project itself. The first, in Section 3.1, will give an overview over the Ultra High Vacuum (UHV) chamber used for the preparation of our sample and its *in-situ* techniques: Auger Spectroscopy (AES), Low Energy Electron Diffraction (LEED) and Physical Vapour Deposition (PVD). The second section (3.2) will deal with the *ex-situ* microscopy techniques used for sample characterisation: Atomic Force Microscopy (AFM) and Scanning Electron Microscopy (SEM) respectively. Lastly, in Section 3.3, we will give a description of the characteristics of the gas-flow setup and the methods used for the Residual Gas Analysis (RGA) of the gas phase during our CO oxidation experiments.

3.1 UHV chamber

The system UHV, shown in Fig. 3.1, consists of two UHV chambers interlocked with each other, and with a single load-lock for the sample loading connected to the preparation chamber. Their base pressure comprises of $10^{-10/11}$ mbar and are constantly being pumped by a series of pre-pump, turbo-pump and titanium sublimation pump.

The first chamber, that serves as a preparation chamber, contains the Ar^+ sputter-gun, oxygen and other gas lines, besides both the Ce and Rh evaporators used in this work. The second chamber, instead, is used as analysis chamber where AES, LEED and the Scanning Tunneling Mycroscope (STM) systems are mounted. Due to the non-conductive nature of the MgO

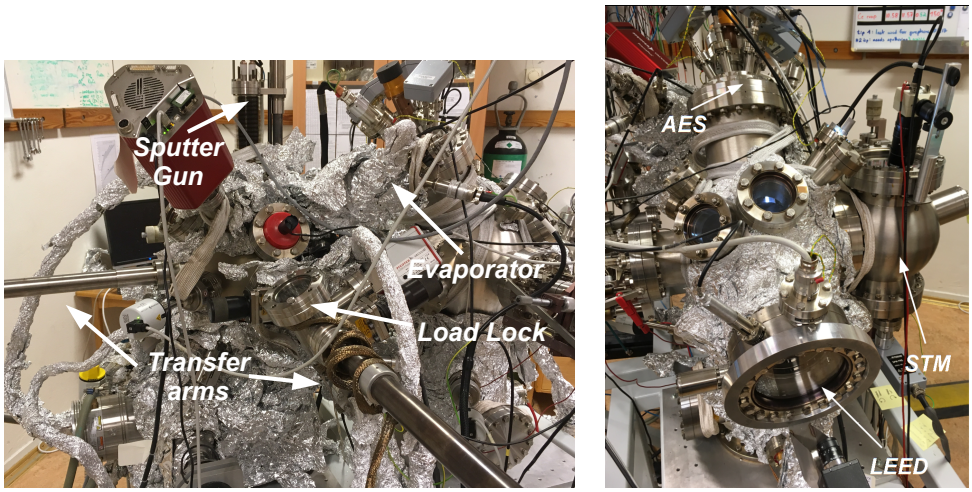

(a) Obelix Prep. Chamber (b) Obelix Analysis Chamber

Figure 3.1: *pictures of UHV Preparation (a) and Analysis (b) chambers in the "Obelix" lab, in Physics Department. In both the important experimental features are highlighted: in (a) are clearly visible the transfer arms using for sample manipulation in UHV environment, the load-lock, sputter-gun and evaporator. On (b) are highlighted the analysis equipment available in-situ: AES, LEED and STM respectively*

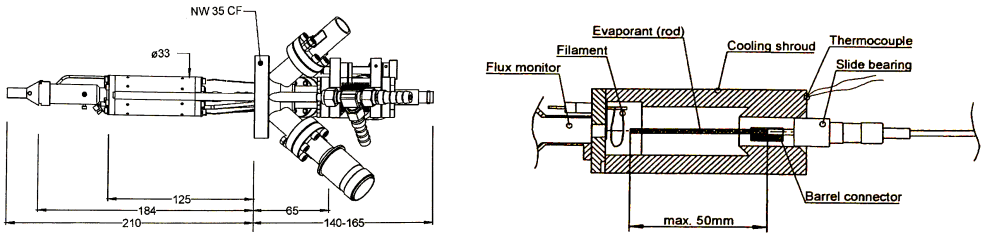

(a) Evaporator schematic (b) Evaporator section

Figure 3.2: *PVD Evaporator schematics, in fig (a) is shown the external schematic of the evaporator with relative measurements and in which can be clearly seen the copper shroud. In fig (b) a vertical section in which are highlighted all the principal components of the instrument* [1]

substrate, with a band-gap of approximately 6 eV, the use of the STM resulted fruitless.

Let's then analyse in more detail the individual techniques correlated with the UHV treatment of our samples.

3.1.1 PVD

Physical Vapor Deposition (PVD) is a technique that can allows the deposition of a material, in this case Rh and Ce, on a given substrate. The first step in the deposition process is the vaporization of the material, usually a metal. Also oxides can be grown dosing oxygen in the UHV during the deposition of the metal component, in so-called Reactive-PVD.

The evaporator set-up, is shown in fig(3.2) and consist mainly of a source of metal, a heating filament, and a current reading collar at the exit of the device. Everything is then enclosed in a copper, water cooled, shroud put in UHV environment.

The heating takes place by mean electron bombardment and once evaporated, the metal, will have an isotropic distribution around the evaporation spot. Due to the geometry of the system, and the differential of pressure created by the exit of the PVD system, a stream of metal is then projected into the chamber through the front aperture, where it sits the collar current-reader. The current, read from the ions generated through this process, gives the value labeled as Flux in tab 4.3. A proportional reading of the actual flux of material through the collar is then generated. Nonetheless, since every material will have its specific "ionization tendency", the instrument have to

[1] image taken from Focus Instruction Manual UHV evaporator EFM 2/3/3s/4, Hunstetten, Germany, June 15

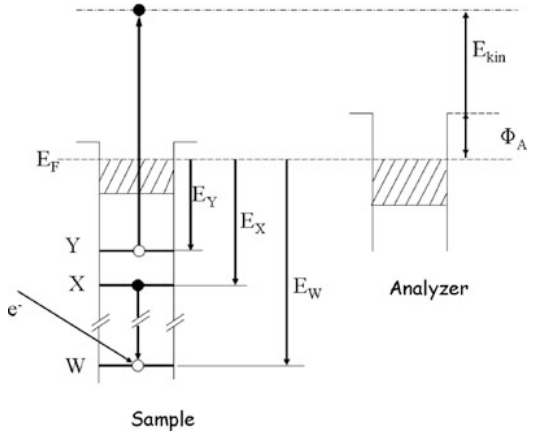

Figure 3.3: *Auger transition mechanism. Here the electronic levels are labelled X, Y and W with their respective energy to the E_F labelled E_X, E_Y and E_W. The work-function is then ϕ_A and the electron kinetic energy E_k* [2]

be specifically calibrated with the aid of a microscopy technique to determine the Å/(Flux·min) .

3.1.2 AES: Auger spectroscopy

The Auger Spectroscopy (AES) consist in a electron-in, electron-out core-level spectroscopic technique. Due to the use of electrons as probe it is highly surface sensitive, with a probing depth of few nm depending on the energy of the out-coming electrons. It can be used both for qualitative and quantitative analysis; employed for both elemental and chemical analysis. [33, 34]

In this work specifically, the AES use will be mainly as a qualitative elemental technique used for sample preparation, and in some limited fashion, for quantitative estimation of metal coverage.

Theory

After an ionization of the target atoms by means of an electron gun, the de-excitation can take place in two different radiant paths: X-ray fluorescence, by the emission of a photon; or by Auger decay: with the emission of a secondary electron. [33]

The Auger de-excitation process (Fig. 3.3), ignite by the removal of a core electron by mean of electron impingement, consists in a decay of a

[2] pictures taken from *Auger and X-Ray Photoelectron Spectroscopy in Materials Science*, S. Hofmann, Springer, 2013

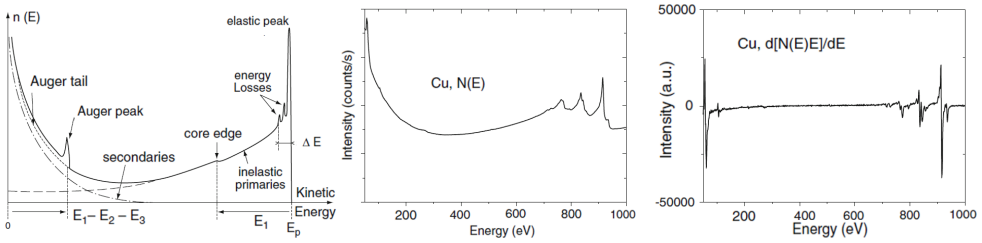

(a) Component schematic (b) AES spectrum (c) Differential AES spectrum

Figure 3.4: *Comparative spectra, for Cu $M_{2,3}VV$ L_3VV Auger peaks, between standard (b) and differential (c) Auger spectra. For further insight on interferences electronic processes, also a schematic (a) view of the different components of the total secondary electron spectrum observed with an AES instrument. Plasmon energy losses (ΔE, shown for elastic peak E_p), an ionization loss (core edge, E_1), and an Auger peak are shown together with the three main parts of the background, consisting of the "Auger tail," of the "true" secondary electrons, and of the inelastically scattered primary electrons.*[3]

upper-state electron into the place of the missing core one. This decay bring to an excess energy that is then dissipated by emission of a secondary electron which E_{kin} is given by:

$$E_{kin} = E_h + E_e + E_s + \Phi \tag{3.1}$$

In which: E_h is the core-hole energy, E_e is the binding energy of the core-hole filling electron, E_s is the energy of the shell from which we have Auger emission, and Φ is the work function of our material.[33]

In particular, thanks to the electron energy-level quantisation, we will have an emission energy which will be based solely on the electronic level as shown in Equation 3.1: obtaining characteristic Auger emissions for each atomic energy level, also called atomic-shells. For this reason, when referring to specific transition, they will be labelled for instance: $KL_1L_{2,3}$. Where the first letter (K) denote the ionized level, the second(L_1) the electron filling shell and the third ($L_{2,3}$) the Auger electron emission level.

Regardless of the energy of the outcoming electron however, due to the short mean free path of the electrons in solids, the technique will be highly surface sensitive: with a probing depth of the order of 10^{-1} - 10^{1} nm (data via NIST database [35]).

One drawback for this high surface sensitivity is the general low Signal-to-Noise ratio caused by the scattered electrons throughout the material and other electronic transitions. To solve these problem, in addition to an

analog-signal enhancement through electron energy analyser and a lock-in amplifying method, the data are also displayed (Fig. 3.4) as a differential $\frac{dN_{(E)}}{dE}$ over E. This approach will ensure a smoothing of the relative constant background against the new, sharp resolved, Auger peaks. [34]

Experimental Setup

For the excitation, a monochromatic electron beam is used with the typical energy around 1,3 KeV, with a focus diameter of approximately 0,1 mm^2 at the sample. The electron analyser consists of a cylindrical mirror analyser (CMA) in a coaxial configuration with the electron gun. The CMA, as stated in the name, consists of a couple of coaxial cylinders on which high voltage is applied in order to act as energy bandpass filter for the channel electron multiplier, that is the electron detector.

To acquire an energy representative spectrum, the electron passing the CMA have to be properly focused. To do so, the sample must be aligned at the correct distance from the AES head. This adjustment is manually operated centering the energy peak, from the elastically scattered electrons with known E_k, to the correct energy on the spectrogram. Once the E_k in calibrated on the spectrogram to the right energy, in this case 1,3 keV, a full spectrum can be registered.

3.1.3 LEED

Low-Energy Electron Diffraction represents a good and quick technique to determine the overall quality and surface structure of a crystalline sample. Being an electron-in, electron-out technique has to be performed in vacuum and it constitutes, one of the instruments mounted on the UHV analysis chamber.

Theory

LEED diffraction can be explained by the electron wave-like behaviour of electrons. With the wavelength of the electron beam determined by De Broglie principle, the diffraction effects will be due to the elastically scattered electrons at the lattice surface. With an energy of 20-300 eV and λ of 2-0.7 Å in fact, the electrons will have approximately the wavelength of the same order of the lattice of reflectant and, as already discussed the short electron

[3]pictures taken from *Auger and X-Ray Photoelectron Spectroscopy in Materials Science*, S. Hofmann, Springer, 2013

elastic mean free path in the materials will ensure us an enhanced surface sensitivity. [36, 37]

To briefly describe the theory behind this technique we can take two different approaches: the first one is just a geometrical consideration about the path difference -P_d- between two waves for constructive interference.

$$P_d = d \cdot sin(\theta); \qquad m\lambda = d \cdot sin(\theta) \leftrightarrow sin(\theta) = \frac{m\lambda}{d} \tag{3.2}$$

Where P_d is the path difference, d is the distance between atomic rows and θ is the angle between incoming and out-coming beam. From this simple approach can be seen how: constructive interference will occur for specific angles.

Another approach consist in considering the problem from the reciprocal space point of view, also called k-space. In particular, the relation between a real lattice vector $\mathbf{R}$ and its reciprocal $\mathbf{G}$. Limiting the model to 2D space:

$$\mathbf{R} = l_1 a_1 + l_2 a_2, \qquad \mathbf{G} = hb_1 + kb_2 \qquad a_i \cdot b_j = 2\pi\delta_{ij} \tag{3.3}$$

Then considering the wave vector $\mathbf{k}$, measurement also of the electron momentum, in the $\mathbf{k}$ space:

$$|\mathbf{k_0}| = \frac{2\pi}{\lambda}; \qquad |\mathbf{k_0}|cos(\theta) = \frac{2\pi}{d}m \tag{3.4}$$

Since we are considering only elastically scattered electrons $|\mathbf{k_{in}}| = |\mathbf{k_{out}}|$; and considering an electron beam perpendicular to the surface $|\mathbf{k_0}|cos(\theta) = |\Delta\mathbf{k}_{||}|$. Therefore:

$$|\Delta\mathbf{k}_{||}| = \frac{2\pi}{d}m \tag{3.5}$$

Finally: d can be written as $d = |a_1| \cdot cos(\varphi)$ where a_1 represent the lattice primitive vector and φ the angle $\widehat{a_1, d}$, while $|\mathbf{k_0}| = |\mathbf{\Delta k}_{||}| = \frac{2\pi m}{|a_1| \cdot cos(\varphi)} = |\mathbf{b_1}|m$. So, implementing this also for a second vector a_2, will give the condition $|\mathbf{\Delta k}_{||}| = |b_1|m + |b_2|n$. Thus, the condition for constructive interference can be shown occuring fo $\mathbf{k}_{||}$ equal to a reciprocal lattice vector, so that:

$$\mathbf{\Delta k}_{||} = \mathbf{G} = hb_1 + kb_2 \tag{3.6}$$

We then have concluded that the LEED pattern will correspond to the surface reciprocal lattice, from which we can directly reconstruct the real lattice.

Even more important consideration for our analysis, dealing mainly with the *quality* of the surface, is on the overall sharpness of the LEED pattern.

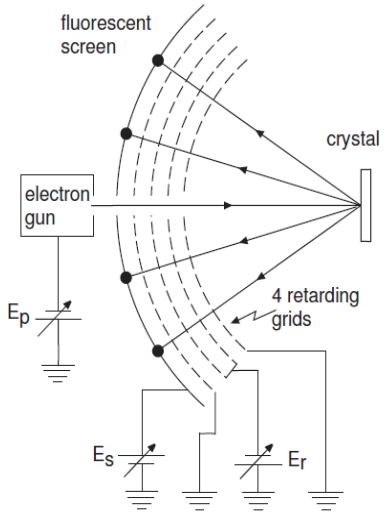

Figure 3.5: *General LEED setup: the electron gun supply electrons with a kinetic energy E_p, that impinging on the sample give Auger decay. The second and third screen generate a field with in order to gain $E_r < E_p$ for non-elastic electron screening. Then the field generated between the last grid and the screen accelerate the electrons to E_s for the final imaging* [4]

In presence of a perfect crystal this will behave as a unique scatterer, so the interference condition will be met in only few point: giving a sharp interference pattern. On the other hand with a lower quality crystal, where there are mismatched reflection-planes, the condition for constructive interference will be met in points slightly misaligned: this will results in a blurred the LEED pattern. So we can generally derive the rule of thumb: the sharper the peaks, the more "mono-crystalline" the surface will be. This point will be of primary concern among sputtering cycles and actual deposition of NPs on MgO (2.2.2, 4.1.1) for improve the possible outcome of the deposition itself.

Experimental Setup

The LEED station, shown in Fig. 3.5, consist of a primary electron source, a series of electrostatic lenses, and a fluorophore screen to visualise the backscattered electrons. Both flux and E_k of the electrons can be varied at the source, and after impinging on the sample perpendicularly, the electrons are backscattered to the electrostatic lenses.

These consist of 4 grids and fluorophore screen at a different voltage, in order to focus and image only the elastically scattered electrons. The

first, from the sample position, is grounded: this in order to not distort the trajectory of the electrons. The second and third have a voltage applied between them, with energy regulated slightly below the energy of the impinging electron: this provides an efficient screen to non-elastically deflected electrons, insuring a better Signal-to-Noise ratio. The last screen purpose is then to accelerate the electrons to the fluorophore screen, usually with a few keV voltage, in order to acquire a sufficiently bright image from the camera pointed at the screen. This simple and efficient method permits both analog observation and digital storage of the LEED pattern.

3.2 Microscopy techniques

In this section the microscopy techniques used to analyse the growth of the NPs, will be presented. Atomic Force Microscopy (AFM) and Scanning Electron Microscopy (SEM) have been chosen as complementary approaches to ensure an overview of the sample characteristics. A theoretical approach to these [38, 39, 9] , especially for what concern aberration and instrumental limitations, will be fundamental for the data interpretation of the following chapter.

3.2.1 AFM: Atomic Force Microscopy

Atomic Force Microscopy (AFM), also called Scanning Force Microscopy (SFM), is a technique that takes advantage of attractive and/or repulsive forces on a probing tip, to determine the topology and in limited fashion also the composition, of the probed sample. Relying on mechanical behaviour from an atomically sharp tip mounted on the end of a thin cantilever, this technique can have different modes of applications depending on the operator requirements. Three main methods can be identified in operation: Contact, Non-Contact and Tapping Mode. Due to the very different mode of operation, the three method take advantage of different approximations in the theoretical description of their behaviour, so that based on the mode used we must analyse the tips' behaviour under different theoretical assumptions.

Due to the specificity of our sample, in particular the presence of abrupt features on the surface as NPs, the Tapping Mode has been preferred over the others: in order not to damage or modify the surface in any way. Then, in the following section, this mode will be the main topic along with some useful technical detail of the instrument itself.

[4]picture taken from *Solid State Physics: an introduction*, P. Hofmann, Wiley, 2015

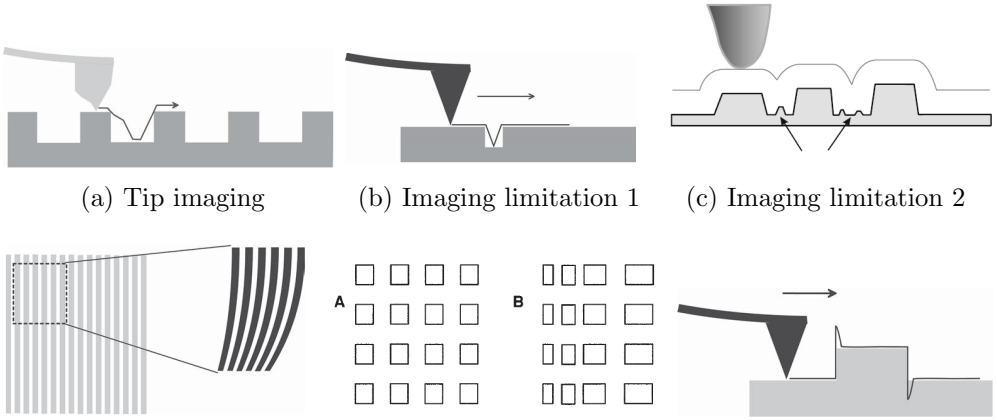

(a) Tip imaging (b) Imaging limitation 1 (c) Imaging limitation 2

(d) Orizontal creep (e) Non-linear piezo responce (f) Z-axis creep

Figure 3.6: *Few of the most common artifacts in AFM image analysis. For what concern tip artifacts, even if the surface presents well spaced and defined features, the shape of the tip could produce direction-specific distortions (a,b), or in case of fine details just not being imaged (c). Scan artifacts are usually connected to piezo non-perfect-linear behaviour on xy-plane (d,e). Z-axis creep (f) will be determined by the reaction time of the AFM electronic adjustments to abrupt features: scan speed and z-range tuning will affect all scan artifact depending on the settings* [5]

Tapping mode AFM

In Tapping mode the oscillation amplitude is usually of several tens on nm. This, in combination with the anharmonic oscillation given by the strong interaction at the sample proximity, brings to the difficult modelisation of this mode under the common harmonic approximation. This approximation, along with linear interaction tip-sample, are used several time in the theory of the other AFM modes: these cannot be used here and a more empirical approach is needed.

Given the tip of the instrument, its oscillation will have a resonance frequency of ω_0 and a free amplitude of A_{free}, with the maximum oscillation given by $2A_{free}$. The measured signals from the instrument are the oscillation amplitude and the phase shift of the cantilever For a free oscillation, the frequency will be the natural resonance frequency ω_0 with amplitude $2A_{free}$. When the tip will come into proximity of the surface, the oscillation will be hampered by repulsive forces, and keeping a nearly sinusoidal oscillation, the amplitude hindering and resonance frequency will have a linear dependency from the distance d tip-sample. [38]

In the AFM imaging, several artifacts are common and a few instrumental limitations have to be taken into account to have a good image interpretation. [39] The most prominent of the instrumental limitation is the problem in imaging possible overhangs on the sample. Due to the physical dimensions of the tip when in presence of an overhang, an imaging of the *"shadowed"* parts are mechanically impossible. The second major limitation is due to the effective sharpness of the tip: even if in theoretical considerations this is atomically sharp, it is usually around few nm in diameter: affecting the resolution power in relation to abrupt morphologic features, as shown in Fig. 3.6.

For what concern the most common artifacts, shown in Fig. 3.6, they can be divided in tips and scan artifacts. The former are due to tip imperfections and shape: resulting in distort features like broadening, shadows and regular distortions. The latter, are mainly broadening of features by non-linear behaviour of the piezos, hysteresis and creep effects due to the non-instantaneous feedback of the system to sample features. [39]

Experimental Setup

The images are acquired with a commercial JPK NanoWizard®4 Nanoscience and with a AFM-tip with a radium <10nm. In this setup a beam deflection method coupled with a thermal determination of spring constant are used for the measurement and calibration of the instrument.

The beam deflection method, consist in the use of deflection of a reflected laser for the determination of the tip movements. In particular, this is evaluated through a contrast function $F = (S_A - S_B)/(S_A + S_B)$ where S_A and S_B are, as shown in fig 3.7, the surfaces on a split photodiode: using this, and some geometrical corrections due to the instrument specific optic, we can determine the relative displacement of the tip.

Since we are working in tapping-mode, that implies the constant oscillation of our cantilever, the precise spring constant of the system has to be determined. To do this we will employ the ambient thermal radiation and asses the natural resonance frequency of the tip. Once selected the right frequency, usually about 70-80% on the shoulder of the maximum amplitude peak, this will constitute the baseline for the software to determine the damping coefficient for the tip-surface interaction.

[5]pictures taken from *Scanning Probe Microscopy*,B. Voigtländer. Springer, 2015 and *Methods in Molecular Biology, vol. 242: Atomic Force Microscopy: Biomedical Methods and Applications*, D. Ricci and P.C. Braga, Springer, 2004

[6]picture taken by *Scanning Probe Microscopy*, B. Voigtländer. Springer, 2015

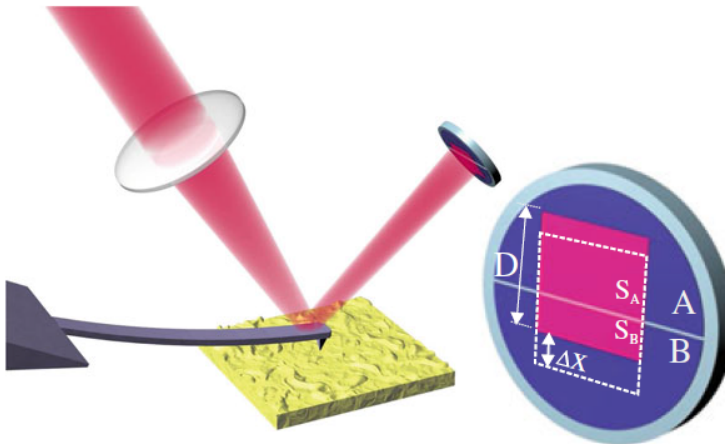

Figure 3.7: *Schematic of laser reflection system for AFM tip displacement measurements. On the right: a front view of the split-photodiode used to retrieve the contrast function* $F = (S_A - S_B)/(S_A + S_B)$ *where the areas* S_A *and* S_B *are marked.* [6]

3.2.2 SEM

Scanning Electron Microscopy is an imaging technique that, employing a focused electron beam, rasters the surface of the target to collect a complete image with spatial resolution up to few nm. As many techniques already presented, being based on electrons as probing medium, this measurement has to take place in UHV environment to acquire a meaningful signal.

SEM can be operated in two main modes: secondary electron detection and back-scattered electron detection. In particular in this work we will focus on the former.

Theory

As the name implies, the SEM is a scanning technique, so that the image is formed not on a 2D detector but on a point detector, where the complete image created rastering the surface in x and y directions. This is an important remark considering the limiting factor for the instrument resolution: for this reason, in fact, in this case it depends only on the spot-size of the impinging beam and the quality of the lenses. Modern SEM could nowadays achieve a resolution up to 1nm^2.

After the impinging of the primary electrons on the surface of our sample,a flux of secondary electron is generated depending on: atomic characteristics, the conductivity of the substrate, geometry and relative impinging angle. For the same argument treated in the AES part, about the electron mean free

path in material, all the generated flux will come from the first few nm of the sample and, if not perturbed by Coulombic effects, it will have specular characteristics to the impinging beam: leaving a trivial task to retrieve the SEM image.

Being a technique based on photoelectric effect, a superficial charging of the sample represent a principal drawback on the use of the technique. In fact, due to the photoelectric effect on the target's surface, poorly conductive samples tend to present major problems of "charging" effects, that will build-up charge by electron scattering, creating Coulombic repulsion between impinging electrons and the surface. In their turn, these electrostatic effects, will generate a non-elastic scattering at the samples' surface, that will invalidate the geometrical assumption for image formation and disrupt the image reconstruction.

Usually, this inconvenient is overcome by coating the sample with a near mono-layer of highly conductive material; obvious to say that this not represents an option in Surface Science. In this case, everything has to be put on the experience of the user and the overall characteristics of the sample.

3.3 Flow-Reactor Setup

In this final section, the second main setup used for this work will be presented, which implementation and trouble shooting was integral part of this work.

Specifically, this consists in a custom built gas-flow system, which schematics can be seen in Fig. 3.9 *(b)*, in its turn composed by a gas-mixing system (Fig. 3.9 *(a)*), a flow-reactor (Fig. 3.8) alongside with a mass spectrometer, used for residual gas analysis (RGA), and a complete vacuum system.

3.3.1 Catalytic Activity

The catalytic activity tests were performed at near ambient pressure, in a flow-reactor supplied by Chalmers, shown in Fig. 3.8, of which comparative results can be seen in ref [24].

In particular, the system is limited to a temperature range from ∼25 C (room temperature) to ∼500 °C, and with a pressure range of 0.05 to 0.8 bar: due to the "open-nature" of the chamber (see Fig. 3.8).

After the dosing of the gasses in the mixing system, and the reaction in the catalysis chamber, the output gasses will be analysed by the mass

[7] pictures taken from: Zhang et al., Rev. Sci. Instr. 86, 033112 (2015); ref [24]

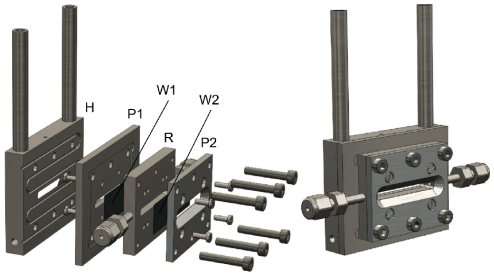

Figure 3.8: *Catalytic flow reactor. In the image an elongated cut-out for positioning the sample can be seen. During the catalytic tests the cut-out was sealed with thick foil (here labeled W1 and W2) and leak tested with He. The "S-shape" groove slotted on the back plate (labeled H) represent the housing for the heating system; in the same plate, through the small hole on top, is also installed the thermocouple for the temperature measurements* [7]

spectrometer: in this case using a Quadrupole Mass Spectrometer (QMS) coupled with Secondary Electron Multiplier (QMS-SEM).

Experimental Setup

To lead the mixture of reactants into the flow reactor cell, a gas-mixing system was used. This, shown in Fig. 3.9 *(a)*, is composed of 6 lines in total: with 4 mass-flow-controllers that can regulate up to 0.7 mL/min for each gasline and 2 that can regulate up to 5 mL/min for Ar lines. In this case, the only noteworthy components in the system is along the CO line: this is in fact equipped with a carbonyl trap Gaskleen II, from PALL, in order to avoid contamination from stripped metal-carbonyl compounds, that otherwise will poison the sample.

As visible in the schematics in Fig. 3.9 *(b)*: from the gas bottles, to the gas system and through the flow controllers, the gasses pass a series of magnetic valves situated right after flow-meters, and then they are mixed homogeneously inside of a mixing chamber, right before the 1/16 inch tube leading to the flow-reactor.

The flow-reactor, shown in Fig. 3.8, consist of a total of 4 stainless steel plates. *H* is the thicker back-plate of the system. On its inside are drilled both the hole used for the thermocouple housing, and the groove used to house the heating wire, that will constitute the heating system used for the catalytic activity experiments. P1, P2 and R instead, constitute the actual

[8]Image partially reproduced from *In situ Structural Studies and gas phase visualization of model catalyst at work*, Sara Blomberg, Lund 2017

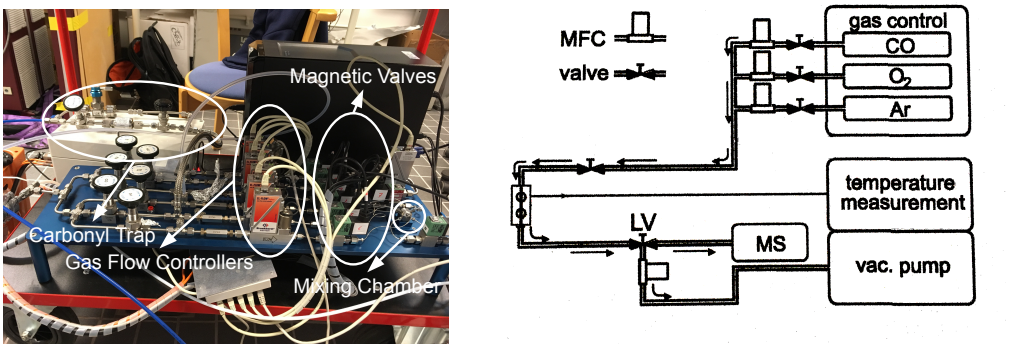

(a) Gas mixing chamber (b) Gas mixing system

Figure 3.9: *Gas mixing chamber on panel (a): well visible the carbonyl trap, gas flow controllers, magnetic valves and gas mixing chamber. In this image, even if not reported, clearly visible one-way valves right before the gas flow controller and the valves used for purging the individual gas lines with the corresponding gas before the actual experiments. On panel (b) a schematics of the complete gas-mixing system: well visible the mass-flow-controllers (MFC), the cell, leak-valve (LV), the mass spectrometer (MS) and the vacuum system.*[8]

"reactor-block": where R is the housing of the catalyst; whether P1 and P2 are the plates that clamp the sealing (W1 and W2 in 3.8) to the reactor, and the reactor itself to the back-plate. As sealant, a combination of both Aluminium 0,05mm and Carbon Foil was used to perform the experiments. No sealant-dependent contribution was noted on the mass spectra.

To complete the setup, after the flow-reactor for the catalytic tests, a further mass-flow-controller up to 250 mL/min, regulating the pressure inside the flow reactor, is positioned.

Finally, connected to the outlet tube with a 1/16 inch diameter, we find the QMS system. This, on its turn, is composed of a HiCUBE pumping station, a PrismaPlus QMG220 mass-spectrometer, both from PFEIFFER, and a cold-cathode pressure gauge for pressure regulation.

Chapter 4

Results and Discussion

In the first part (4.1) of this chapter the differences in sample-preparation dependent-particle growth of three model catalyst samples will be presented. Then, in Section 4.2, we will make a comparison of the microscopy images and the obtained morphology for each sample. Finally, in Section 4.3, we will focus on the catalytic activity during CO oxidation for one the samples for various CO_2/O_2 gas-ratios, and compare it to the results obtained on Pd/Al_2O_3 powder catalyst.

4.1 Details on the sample preparation

During this work, a total of three sample has been prepared with slightly different deposition parameters and settings. These, from now on, will be referred to as: MgO1, MgO2 and MgO3. More details will be added in the following chapter, but brief comparison of substrate and achieved results can be seen in 4.1.

The substrate for all the samples will be of MgO(001), supplied by Mateck,

Table 4.1: *S*amples overview and general morphological results obtained using identical substrate with different deposition parameters. The assigned names will be used in the description along all this chapter

Name	General Composition	Morphology
MgO1	MgO + Rh	NPs + MPs
MgO2	MgO + Rh	NPs
MgO3	MgO + Rh + CeO_x	NPs

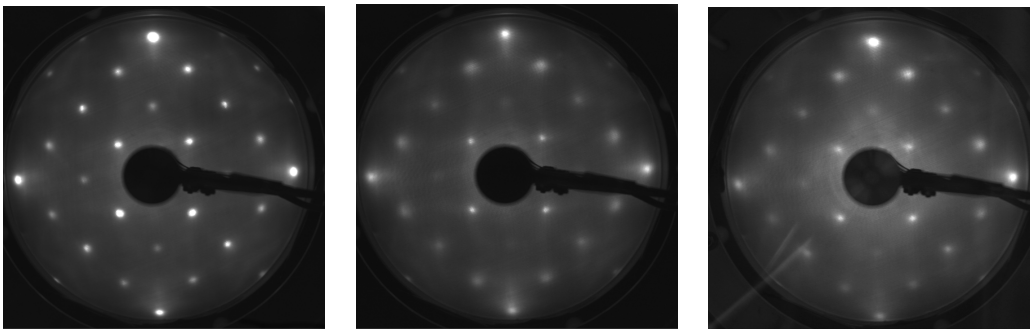

(a) 0^{th} cycle (b) After 1^{st} cycle (c) After last annealing

Figure 4.1: *LEED on MgO1 substrate. In fig (a) as-obtained before treatment: the sharpness and regularity of the LEED pattern is the signature of an excellent surface crystallinity. After the first, very energetic sputtering cycle, blurred features are visible in fig (b). Finally, it can be seen how after a high-temperature annealing cycle, the quality in fig (c) shows partial recovery. All the LEED patterns have been taken at 252eV; (a) and (b) have been equalised with respect to (c) due different exposure times*

in slabs of 10x5x1 mm^3. The sides are cut along crystallographic <100> and <010> axis, with miscut <0,1°.

4.1.1 Substrate preparation MgO(001)

The as-obtained MgO(001) substrates were analysed by LEED and AES to determine the surface quality and chemical composition, to check for potential contaminations. Fig. 4.1 *(a)* shown LEED pattern of such an as-obtained substrate, measured on sample MgO1. For all the samples, the sharp peaks from the LEED showed a good surface quality, with limited surface roughness. From the AES, on the other hand, a non-negligible carbon adsorption was observable in each case: as it can be seen in Fig. 4.2, in which is highlighted the KLL transition, at 272eV, from the absorbed carbon on sample MgO2.

As mentioned in Section 2.2.2 in chapter 2, the surface quality and cleanliness is of capital importance for the deposition outcome. For this reason, we proceeded with mild Ar^+ sputtering at 500 eV to remove the carbon. Fig. 4.2 shows how, with this procedure, we could completely remove the carbon contamination from our samples.

Subsequent to sputtering, all MgO substrates were annealed at an oxygen pressure of 10^{-7} mbar, with other specific parameters reported in table 4.2 This technique, enhancing the surface diffusion coefficient by means of thermal

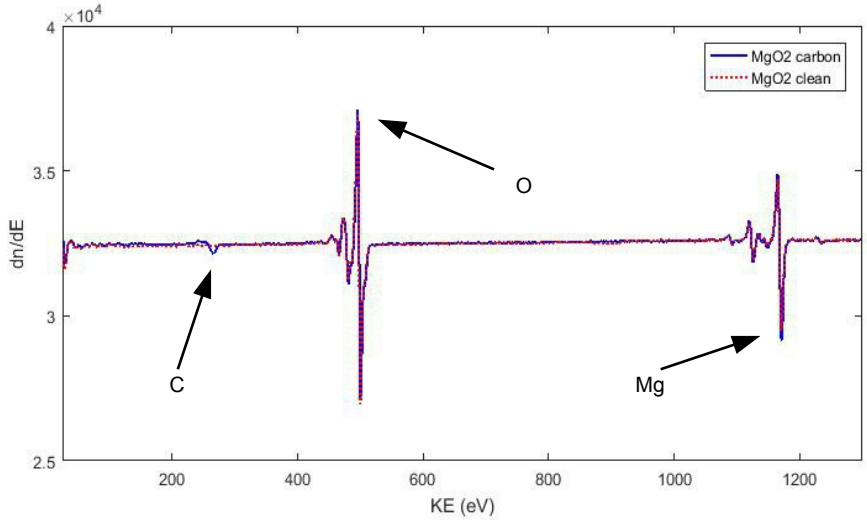

(a) Comparison before and after carbon removal

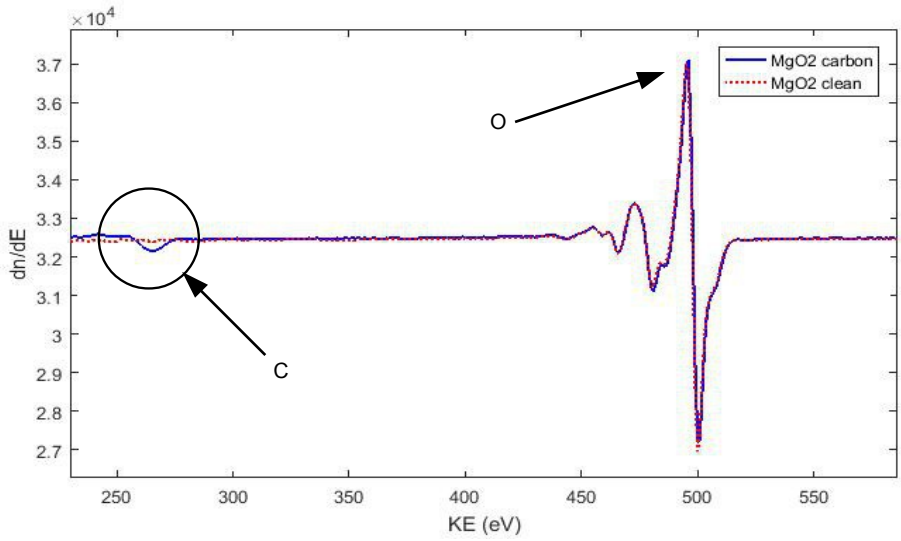

(b) Close-up on carbon peak

Figure 4.2: *Comparison of AES spectra, measured on sample MgO2, before and after carbon removal. (a) shows the whole spectrum with highlighted carbon, oxygen and magnesium peaks. (b) shows a close-up on the carbon peak, with the oxygen peak to the far right as intensity comparison*

Name	Voltage (keV)	Current (mA)	Time (min)	Annealing (°C)	Ann. Time (min)
MgO1	1	10	30	550	30
	1	10	30	550	30
	-	-	-	830	40
MgO2	0.5	10	30	550	30
	0.5	10	30	550	30
MgO3	0.5	10	30	520	30
	0.5	10	30	630	30

Table 4.2: *Sputtering and annealing parameters used during sample preparation. The sputtering process was performed at a stable pressure of 2x10^{-6} mbar of Ar, while for annealing the O_2 pressure was stable at 1x10^{-7} mbar*

energy, speeds up the phenomena of surface smoothing. Moreover, the use of oxidizing atmosphere will ensure the removal of the carbon from the surface as CO/CO_2.

To obtain a comprehensive overview though, since any substrate has undergone a slightly different preparation cycle, an overview is given in the table 4.2:

Multiple cycles of both sputtering and annealing have been required because of the difficulty to obtain a carbon-free surfaces, a basic requirement for good and homogeneous surface on which to deposit. The presence of carbon has been checked at each sputtering/annealing cycle with *in-situ* AES: the sputterings were stopped only after no carbon was visible in the AES spectra.

Noteworthy is that the cycles parameters, in turn, will deeply affect deposition outcomes, as presented in the surface characterization Section 4.2 and specifically for what concern sample MgO1. Therefore, due to different preparation settings, this sample will present peculiar surface characteristics.

MgO1

As mentioned before, the MgO1 sample constitutes an interesting and special case because of the consequences of the harsh sputtering that has undergone in contrast to MgO2 and MgO3.

As can be seen from the LEED spectra of Fig. 4.1, the surface quality deteriorated considerably from pattern *a* to *b*, before and after the sputtering cycle respectively. Pattern *c*, recorded after 40 min of annealing at 830 °C,

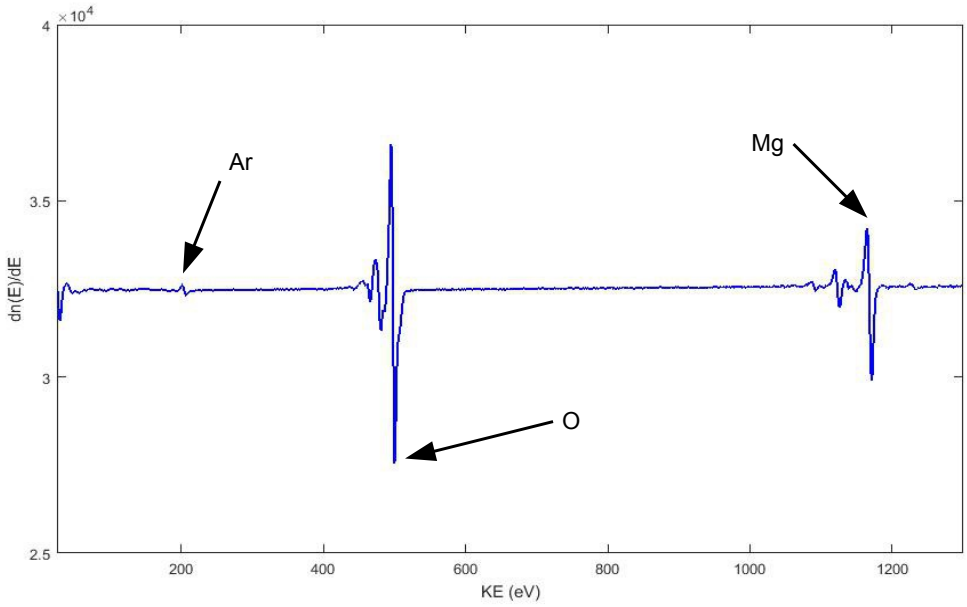

Figure 4.3: *AES spectra showing clearly the Ar signal from the embedded Ar in sample MgO1.*

show a partial recovery with a little improvement of surface quality; even if not recovering completely the initial quality. The AES spectrum shows in Fig. 4.3 a sharp peak at 200-215 eV, that has been identified as Ar LMM peak. This clearly shows how, given enough energy, Ar atoms can be embedded in the crystal surface, with all the possible consequences of which we already extensively discussed in Section 2.2.2. This was the reason for the third annealing cycle at 830 °C for 40 min, as can be inferred from Table 4.2.

4.1.2 Rh and CeO_x deposition

Based on previous works on Rh and CeO deposition [17, 40, 41, 27], we used the values reported on Table 4.3 for deposition.

As discussed in Chapter 2.2.2, the Rh flux and sample temperature are crucial parameters in order to obtain a homogeneous particle distribution. The temperature, in particular results fundamental because it triggers the ripening processes that will ease NPs formation on the surface, instead of a "mirror finish" deposition at room temperature.

Similarly, in the case of CeO_x, we introduce another important variable: the O_2 pressure. In fact in such a reactive PVD process, the balance between $Ce_{(m)}$ deposition rate, O_2 pressure and temperature is what will determine the success of the process itself. Due to the high number of variables involved and the impact of subtle variable oscillations, the aforementioned parameters are usually empirically determined. Specifically for this purpose, as mentioned at the beginning, the need for a references such as [17, 40, 41, 27]

Fig. 4.4 shows the AES spectrum measurement after Rh and CeO_x growth. Therein, we can clearly see the atomic fingerprints of the different components. The relative intensities in particular, besides the position of the peaks that allow the elemental analysis, are noteworthy. In fact, being the AES a surface sensitive technique, this will enhance the signal from the top components, such as Rh and Ce, while suppressing O and Mg which Auger electrons are attenuated from the Rh/Ce layer on top. In particular, we can notice a strong signal from Ce NOO at 84 eV and Rh MNN at 280 eV. While the O KLL at 535 eV and Mg KLL at 1170 are strongly suppressed if compared to the signals from Fig. 4.3

Then, after the deposition cycles, we performed AFM and SEM to characterise the samples. The results will be discussed in 4.2.

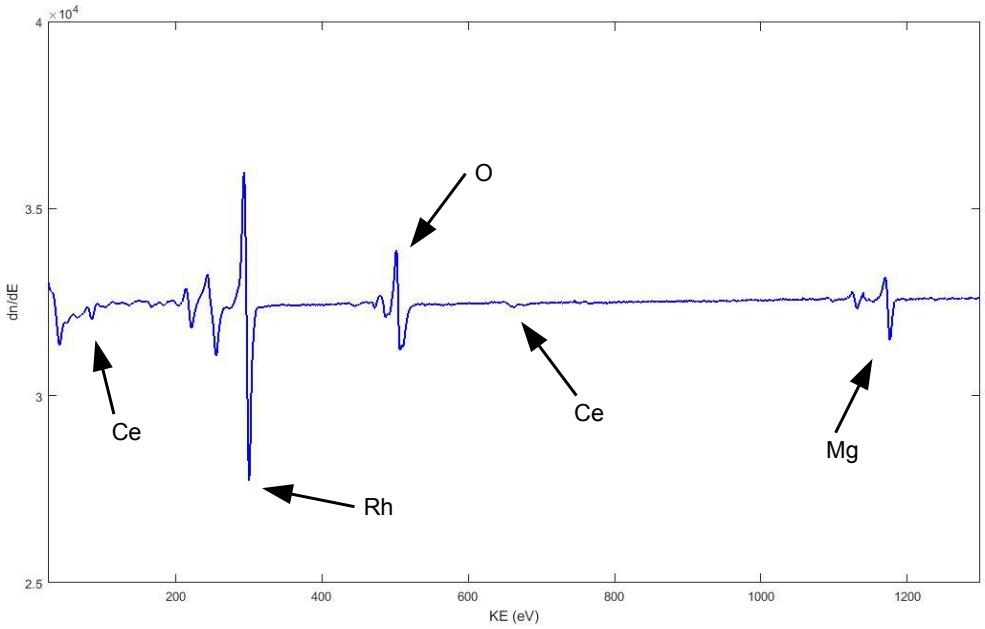

Figure 4.4: *AES spectrum measured on sample MgO3, where all the different components are clearly visible. Ce peaks are present at 664 eV (MNN) and at 84 eV (NOO). O KLL peaks are at 535 eV, whereas Mg KLL is at 1170 eV. Rh MNN peaks instead are at 280 eV*

Name	Rh Flux (nA)	Depos. Time (min)	Temp. (°C)	Ce Flux (μA)	Depos. Time (min)	Temp. (°C)
MgO1	100	25	420	–	–	–
	200	60	420	–	–	–
MgO2	160	150	420	–	–	–
MgO3	110	150	470	1.2	12	500

Table 4.3: *Deposition parameters for both Rh and CeO_x. MgO1 and MgO2 have undergone only Rh deposition, whereas MgO3 both Rh and CeO_x. The O_2 pressure during Ce evaporation was 6x10^{-7} mbar*

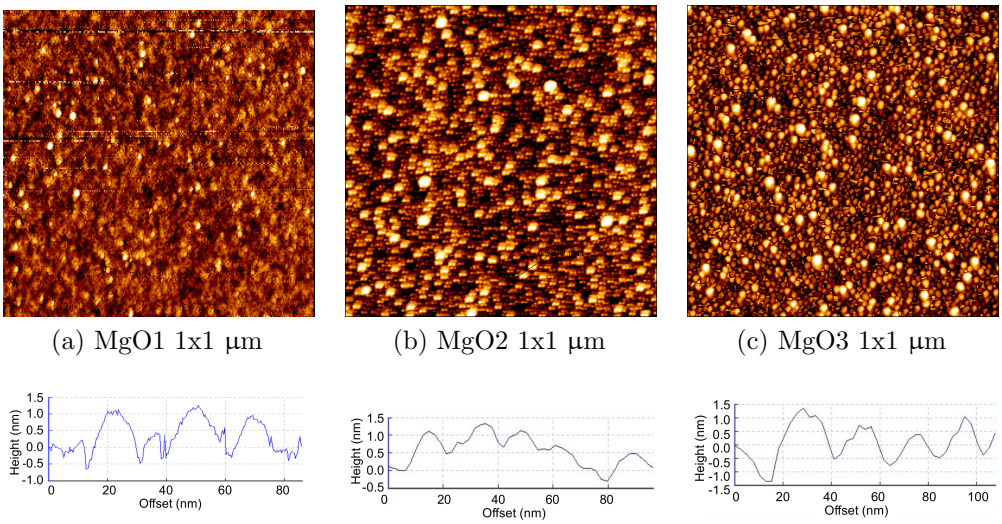

(a) MgO1 1x1 µm (b) MgO2 1x1 µm (c) MgO3 1x1 µm

(d) cross-sections (a) (e) cross-sections (b) (f) cross-sections (c)

Figure 4.5: *Comparison of AFM images of the approximately same resolution. A rather homogeneous particle distribution has been achieved for all samples. (d), (e) and (f) are the cross-sections obtained from the correspondent AFM measurements: confirming the homogeneity of the NPs achieved during Rh deposition*

4.2 Surface characterisation

In the following we will discuss the growth and characteristics of the as-prepared particles on all the samples based on AFM and SEM studies. The first part will focus mainly on sample MgO2 and MgO3, that have been prepared with the same procedure and similar parameters. A separate subsection will discuss sample MgO1, since in its case the harsh Ar^+ sputtering resulted in unique features during deposition.

4.2.1 Characterisation

All samples have been characterised by AFM, and SEM as a cross reference. Because of the drastic difference between these two probing techniques, this complementary approach is designed to confirm the as-obtained data using different means of investigation, in order to gain a more comprehensive and reliable picture of the samples' surface.

Fig 4.5 shows a comparison, via AFM images, of the three samples MgO1 to MgO3 from left to right on the same 1x1 µm scale. As it can be seen from *(d),(e),(f)* there is no substantial difference in particle size and distribution

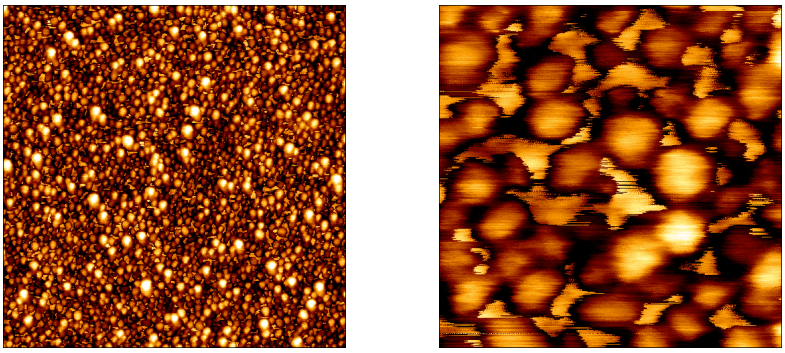

(a) MgO3 1x1 µm (b) MgO3 128x128 nm

Figure 4.6: *AFM images with frame size of 1x1 µm (a) and 128x128 nm (b) for sample MgO3.*

for all three samples, at least at this scale. It is also interesting to note that, despite the high temperature employed during CeO_x deposition, no sign of particle sintering can be observed on MgO3 (Fig. 4.5 *c* and *(f)*)

In the case of MgO3, no particular morphology differences in both AFM and SEM were noticeable. But the overall tendency of this sample to develop less charging effect in the SEM measurements was remarkable. Given the low amount of CeO_x deposited, and the pre-existing "wrinkled" surface of the substrate from Rh deposition, two main hypotheses can be made concerning the CeO_x final distribution. The first one, more likely, is the filling of the gaps between Rh NPs by mean of CeO_x. This could also partially explain the observations with the AFM. As mentioned in Section 3.2.1, the instrument response is also material-dependent other than distance-dependent: in fig 4.6 *(b)* and 4.5 *(c)* can be seen a multitude of what appear to be z-axis creep artefacts (Fig. 3.6 *(f)*) around the NPs bed.

The second one, instead consists in a homogeneous thin deposition on the Rh surface, but due to thermodynamics of nucleation (Section 2.2.2) this seems to be unlikely.

Finally, even if it is consistent with the premises of these types of errors, a stronger contribution deriving from CeO_x can not be excluded. Moreover, the very limited amount of CeO_x deposited in conjunction with the AFMs' typical lack of resolution in the overhangs, bring us to the need of further scrutiny before reaching a final conclusion upon CeO_x local distribution.

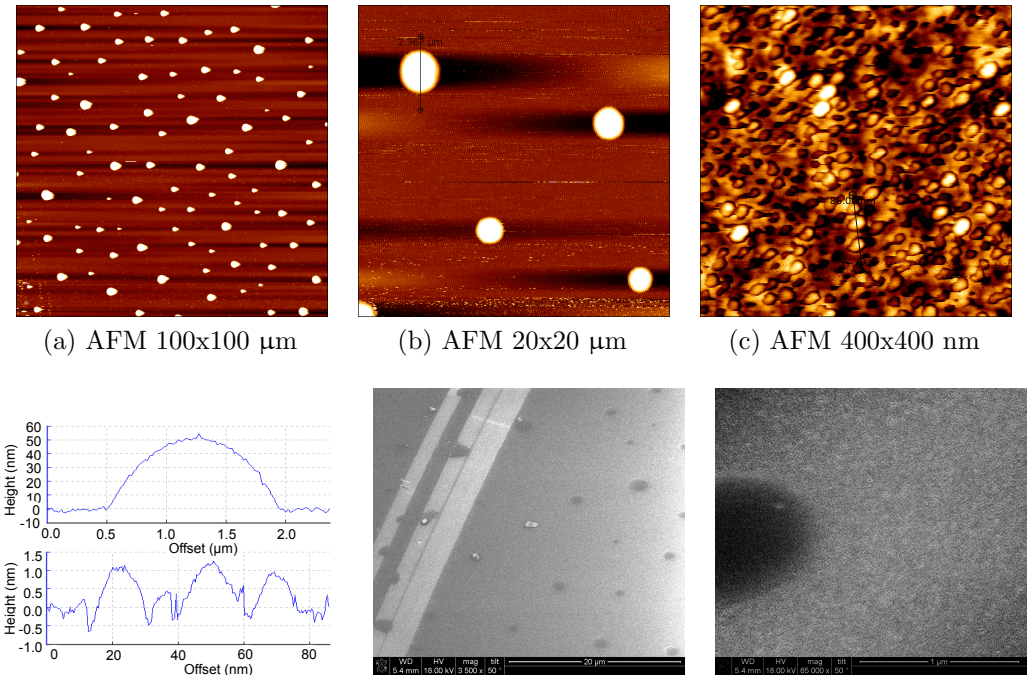

(a) AFM 100x100 µm (b) AFM 20x20 µm (c) AFM 400x400 nm

(d) cross section of *(b)* and *(c)* (e) SEM 1 (f) SEM 2

Figure 4.7: *AFM and SEM images measured on MgO1. Fig* (a) *to* (c) *are the AFM images measured at different scales, showing the different textures of MgO1 depending on the observed scale.* (d) *displays two cross sections from* (b) *on top and* (c) *on the bottom, respectively Finally* (e) *is a SEM image of a scratch present on the surface where clearly the "base" of nucleation for some MPs is visible. While on* (f) *a SEM image of the side of a MPs is imaged, and contrast enhanced, where the general texture is produced by the NPs bed*

MgO1

In the case of sample MgO1, the most interesting characteristic is the coexistence of a complex system micro- and nano- particles. As can be seen from Fig. 4.7 *(b)*, which shows an overview of a much larger scan area, on top of MgO1 is present a homogeneous pattern of MPs among a more abundant NPs "bed". Fig. 4.7 moreover shows a comparative look between AFM and SEM, as can be seen in *(b),(e)* and *f*. Due to SEM specificity, which we discussed in Section 3.2.2, its easy to distinguish between the MgO substrate and the Rh on top: with MgO brighter in the displayed Fig. 4.7*(e)* against darker Rh particles.

In the SEM image, it can also be seen how is clearly visible a scratch, produced after Rh deposition, and inside of which can be seen the base of

removed MPs. This suggests that the origin of this "seeded" growth phenomenon is to relate to defect's sites left from high energy Ar^+ impingement. Moreover, assuming the scratch present to be flush with substrate, this will show that the "seed" site is a "macroscopic" impact crater in which Rh have preferentially deposited, rather than a singular atom vacancy or minor defect.

Considering the Rh deposition parameters we can also argue that the third annealing cycle, due to its high temperature and long duration, may have favoured diffusion phenomena enhancing MPs growth. Nevertheless, comparing NPs size distribution between the two samples, from Fig. 4.5 and 4.7 *(e)* and *(f)*, no evident sintering processes are present on the surface: so this last argument partially loose its validity. Nonetheless, even having high-resolution AFM and SEM images of the surfaces, the data are still too coarse to identify single facets: so no definitive crystallographic-accurate observation is available yet.

Finally, to obtain statistical data, we used a contrast function in the vectorial image processing program (ImageJ). The analysis showed that MPs account for around 8% of the total coverage, with an average diameter of 1,5 µm and height of 50 nm, where the cross-section obtained was by the "height" profile from the AFM. The NPs, on the other hand, show an average diameter of ∼20 nm and ∼ 1.5 nm height. An example for the cross-section for both MPs an NPS can be found in 4.7 *(d)*. To note that even if from AFM scans no free surface is visible, due to tip artifact discussed in Section 3.2.1 and specifically limitation due to tip size of around 10nm, a complete size determination is not yet available.

4.3 Catalytic activity

In the following section the catalytic activity for sample MgO1 and a reference sample, that from now on will be referred as Pd/Al_2O_3, will be discussed. Specifically, the latter consisting of a traditional powder catalyst of Pd on Al_2O_3 in form of a compressed pellet.

As anticipated in Section 2.2.2, the hyper-surface of the reaction, due to its many variables, is rather vast. For this reason we decided to limit the amount of probing points to a few per variable. This will be done setting up a constant pressure and gas-ratio, regulating the respective fluxes, and steadily increasing the temperature: this procedure was repeated for four different gas-ratios on each sample. Moreover, even if not reported in the mass spectra, the cell has been conditioned every time for a few minutes in the chosen gas mixture at ambient temperature before beginning the heating cycles. This has been done to induce the surface in a steady-state point before varying

the system parameters, in order to ultimately gain a reproducible base-point for each experiment.

We tested four different CO/O_2 gas-ratios, from highly CO-rich to highly O_2-rich, as shown in Table 4.4. Specifically, CO7O7 and CO7O4 are the highly and slightly oxidising atmospheres, while CO7O1 and CO7O3 represent highly and slightly reducing atmospheres. This procedure is ultimately performed in order to explore the kinetics of the reaction in a wide range of reducing/oxidizing atmosphere and determine the sample's overall behaviour.

4.3.1 CO oxidation

All experiments were conducted at a total flux of 5 mL/min and 800 mbar of pressure. We used CO/O_2 as reactants and Ar as the carrier gas. Given the net reaction mechanism (4.1) we used gas-ratios for the experiments as shown below in Table 4.4.

$$CO + \frac{1}{2}O_2 \rightarrow CO_2 \tag{4.1}$$

Table 4.4: *CO oxidation parameters. The pressure in all the experiments, for both MgO1 and Pd/Al_2O_3 was kept at constant 800 mbar. The column "Name" corresponds to the name coding used throughout this chapter. In column "Atm." is reported the Red/Ox overall condition for the environment in the reactor*

Name	Ar Flux (mL/min)	O_2 Flux (mL/min)	CO Flux (mL/min)	Total Flux (mL/min)	Gas ratio ($CO:O_2$)	Atm.
CO7O7	3.6	0.7	0.7	5.0	1:1	Highly Ox.
CO7O4	4.0	0.4	0.7	5.0	7:4	Slightly Ox.
CO7O3	3.9	0.3	0.7	5.0	7:3	Slightly Red.
CO7O1	4.2	0.1	0.7	5.0	$1:\frac{1}{7}$	Highly Red.

The column "Stoichiometric ratio", refers to four gas flow combinations chosen according to the stoichiometry of the net reaction. In particular the slightly oxidizing and reducing atmospheres,7:4 and 7:3 CO/O_2 respectively,

were chosen in order to acquire more data-points and more resolution where, by theory, the CO_2 production has its tipping point. In fact, being the system in nearly stoichiometric conditions, should be less affected by the "reagent limitation" effect that could otherwise arise in an environment away from stoichiometric equilibrium.

In the following plots, are shown the signal generated for each gas, corresponding to a given molecular mass, as the raw data provided from the mass spectrometer. The monitored masses were limited to the few of interest in order to gain a better time resolution on the mass spectrometer. This procedure was chosen because, since for every mass scanned the instrument have to selectively and systematically adjust the pass-filter to the Second Electron Multiplier. Reducing the number of analysed point will then reduce the time to gain a complete reading of the chosen masses.

$\mathbf{Pd/Al_2O_3}$

This reference sample has been used since it represents a classical powder catalyst, and accordingly, a "golden standard" in terms of behaviour for catalysts during of CO oxidation. [7, 5, 21, 10, 8, 9]. The spectra for all the experiments are shown in Fig. 4.8, in increasing order of oxidising atmospheres.

In panel *(a)* can be seen the mass spectrum corresponding to experiment CO7O1. At the beginning, the sample is at room temperature, and the signals correspond to the incoming flow of reactants. This is because at ambient temperature, there is no significant ongoing catalytic reaction. At increasing temperature, is registered a gradual rise in CO_2 signal as the catalyst becomes more active; while CO and O_2 decrease correspondingly. The light-off of the sample, at the beginning of the MTL plateau, is at around 320°C. Here, CO_2 is at its maximum, while there is a consistent decrease in O_2 and CO. As expected, these decreases in CO and O_2 signals are to be attributed to the catalytic oxidation of the CO, following the aforementioned net reaction mechanism 4.1.

Experiment CO7O3, reported in panel *(b)*, show a similar behaviour compared to CO7O1, but with a lower light-off temperature, at around 270°C, where the lower light-off temperature can be explained by the higher oxygen partial pressure on the sample. At the same time, it shows also some oscillatory artifacts during all the registered spectrum well visible between 2000 s and 2500 s, where these oscillations can be interpreted as pressure artifacts. This is the case since the corresponding oscillations are also shown in the Ar signal: confirming the fact that this oscillatory behaviour shows a global pressure fluctuations rather than a real oscillatory behaviour of the

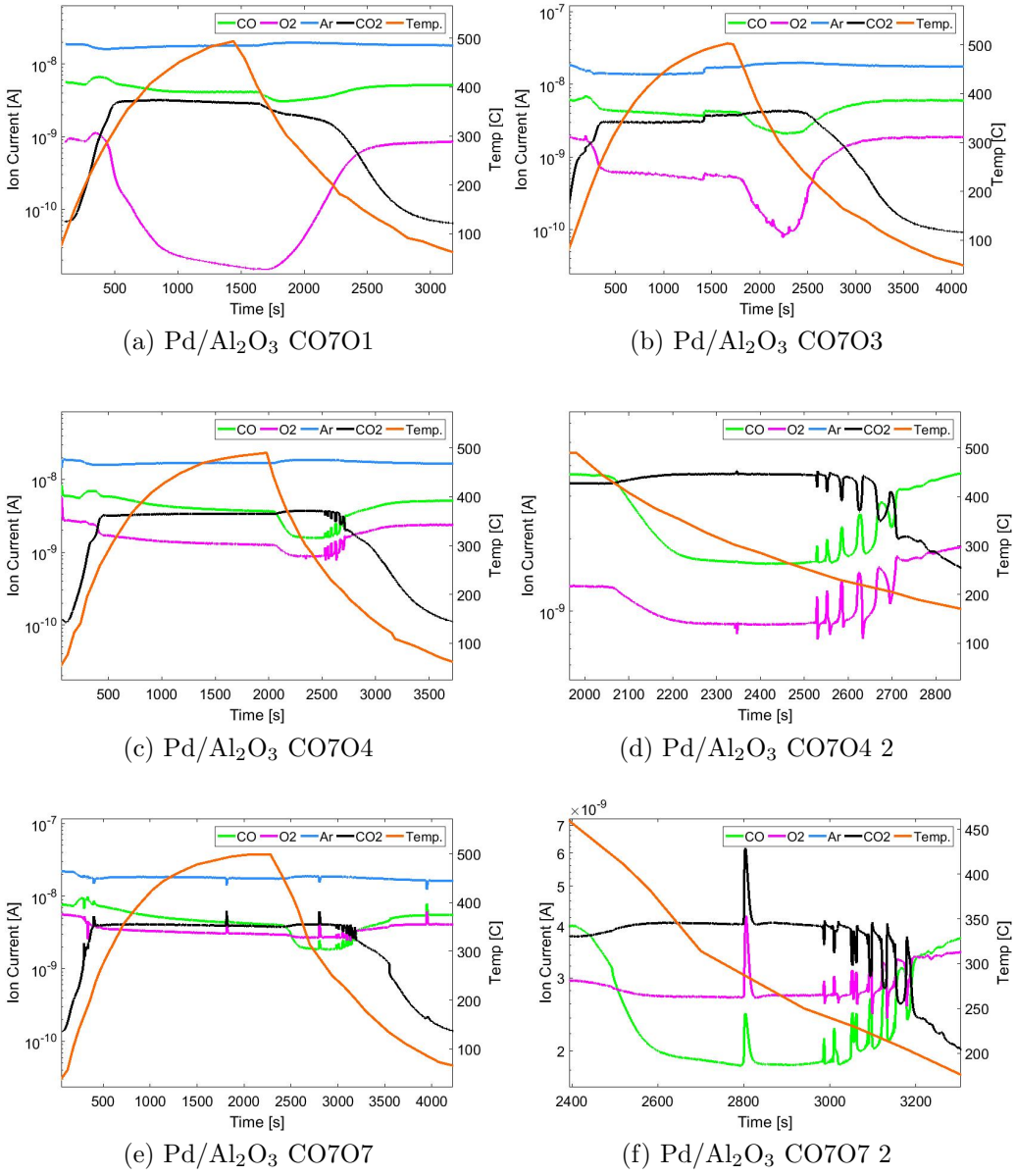

(a) Pd/Al_2O_3 CO7O1 (b) Pd/Al_2O_3 CO7O3

(c) Pd/Al_2O_3 CO7O4 (d) Pd/Al_2O_3 CO7O4 2

(e) Pd/Al_2O_3 CO7O7 (f) Pd/Al_2O_3 CO7O7 2

Figure 4.8: *CO oxidation mass spectra for Pd/Al_2O_3. The results are presented in growing oxidating atmosphere: (a) is CO7O1, (b) is CO7O3, (c-d) are from sample CO7O4 with (d) being a close-up of the 2000-2800s section of (c). Similarly (e) and (f) are a complete scan of CO7O7 and its respective close-up in 2400/3300s segment. In the spectra: in orange the temperature, black line corresponding to CO_2. Ar is in light-blue, whether O_2 in magenta, concluding with CO in green. All the plots are presented as IonCurrent[A] and Temperature[°C] against Time[s]*

catalytic activity.

Following, in panel *(c)* experiment CO7O4 is shown, and in *(d)* its cropped section between 2000 s and 2800 s. Generally, a similar behaviour to the previews two spectra is shown, with a light-off temperature at around 270°C. The oscillations of CO7O4, cropped in panel *(d)* between 2600 s and 2800 s, have a relative temperature interval between 250°C and 210°C. This oscillatory phenomenon, already known in literature as "self-sustained" oscillations [14, 30], has been also discussed in 2.1.3, and will be explained more in detail the following paragraph.

The detailed catalytic cycle, involved in the aforementioned self-sustained oscillations, can be seen in Fig. 4.10 *(a)*. Here, at the beginning of the cycle in 1, at room temperature, the metallic surface is being completely covered by the CO. This is due to the fact that, at room temperature CO have an higher absorption energy with respect to O_2 to the catalysts' surface, favouring its preferential chemisorption. At this stage, no O_2 molecule can reach the surface, and consequently the reaction is prevented. During passage a, the raising temperature, gradually promotes the kinetic desorption of CO from the Pd surface, and in turn it increases the CO_2 production via a Langmuir-Hinshelwood mechanism [14]. This, continues with higher activity corresponding to higher temperatures, until the light-off of the catalyst. At the light-off, the total amount of oxygen absorbed on the surface is enough to catalytically remove all the CO, as showed in step 2. Here, during b, the reaction continues in the MTL regime, while contemporary starting to build a thin oxide layer on top of the metallic catalyst. This thin layer of oxide, created by the surface exposure to the reactive O_2 in the reactor, does not hamper the reaction [14] nonetheless, while the reaction proceed through c, a thicker oxide is formed. Consequently, in step 4, a thick and catalytically less active oxide is present on the catalysts' surface. In turn, with a lower catalytic activity, the CO concentration rises and a Mars-van-Klevelen mechanism [14] slowly start to consume the newly formed oxide, during passage d. Once all the oxide is consumed, a rough metallic surface is left by the reduction mechanism in step 5. On such a defect-rich surface, the binding energy CO-substrate result higher compared to the energy in step 1, because of the higher interaction of CO with low-coordination Pd atoms. This, then, once again brings the deactivation of the catalyst. Finally, during e, a thermal-activated reconstruction process smooth the metallic surface of the catalyst, restoring the initial condition and fostering a new cycle.

Noteworthy is also the fact that similar situation can be found also in CO7O7, in Fig. 4.8 *(e)* and *(f)*. Here the catalytic behaviour is similar to the previous case, with the only difference that, once more due to higher O_2 partial pressure, both the light-off and the oscillations are observed at a lower

temperatures. In this case in fact, the light-off happens at around 190°C, while the oscillations between 240°C and 220°C.

Concluding, it can be seen how these observations are in line with the literature available for this catalysts' family. As it can be noted from the relative slopes for CO_2 signal, for all the gas ratios, that an MTL plateau is reached fairly quickly; even in O_2-poor/CO-rich conditions. This behaviour then confirms the extremely high catalytic activity typically observed for Pd catalysts. [31, 14, 30, 21]. Moreover, in O_2-rich conditions, in experiment CO7O4 and CO7O7, an oscillatory behaviour of the catalytic activity is observable: coherent with the self-sustained oscillations as reported in recent articles [14, 30].

MgO1

The following section will present an analysis for MgO1 under the same conditions as for Pd/Al_2O_3. The mass spectra corresponding to MgO1 are shown in Fig. 4.9.

Similar to the previous sample Pd/Al_2O_3, it can be seen how the light-off temperatures of the Rh catalyst are lowering with increasing oxidizing atmospheres. More specifically, we determine the light-off temperature at about 375°C for CO7O1, shown in panel *(a)*, and at around 340°C for both CO7O3 and CO7O4, shown in panel *(b)* and *(d)* respectively.

The most prominent characteristic in this series of experiment though, is the presence of oscillation during catalytic activity in CO-rich conditions. Specifically, this take place for experiment CO7O3 shown in panel *(c)*, in the time interval between 710 s and 765 s and with a temperature interval between 345°C and 365°C.

Our interpretation of these oscillations is a non-equilibrium mechanism involving CO-coverage of the metallic surface, as visualised in Fig. 4.10 *(b)*. Given the high CO partial-pressure and its preferential chemisorption compared to O_2[14, 30], a complete CO-coverage of the sample at low temperatures can be assumed, in step 1. With increasing temperature, a kinetic desorption of CO along with catalytic oxidation, shown in passage "a", allows the catalytic dissociation of oxygen at the surface: boosting the catalysis rate and depleting even more, the already O_2-poor atmosphere nearest to the sample, in step 2. At this stage, in the step 3, the catalyst reaches its peak of activity, consuming all the oxygen on the immediate samples' surroundings. This, allows new CO molecules to adsorb at the surface, in passage "c", blocking once again the surface. The catalyst is then deactivated once more, until the surrounding atmosphere does not reach a sufficiently high O_2 composition to favour its dissociation on the catalysts' surface. This

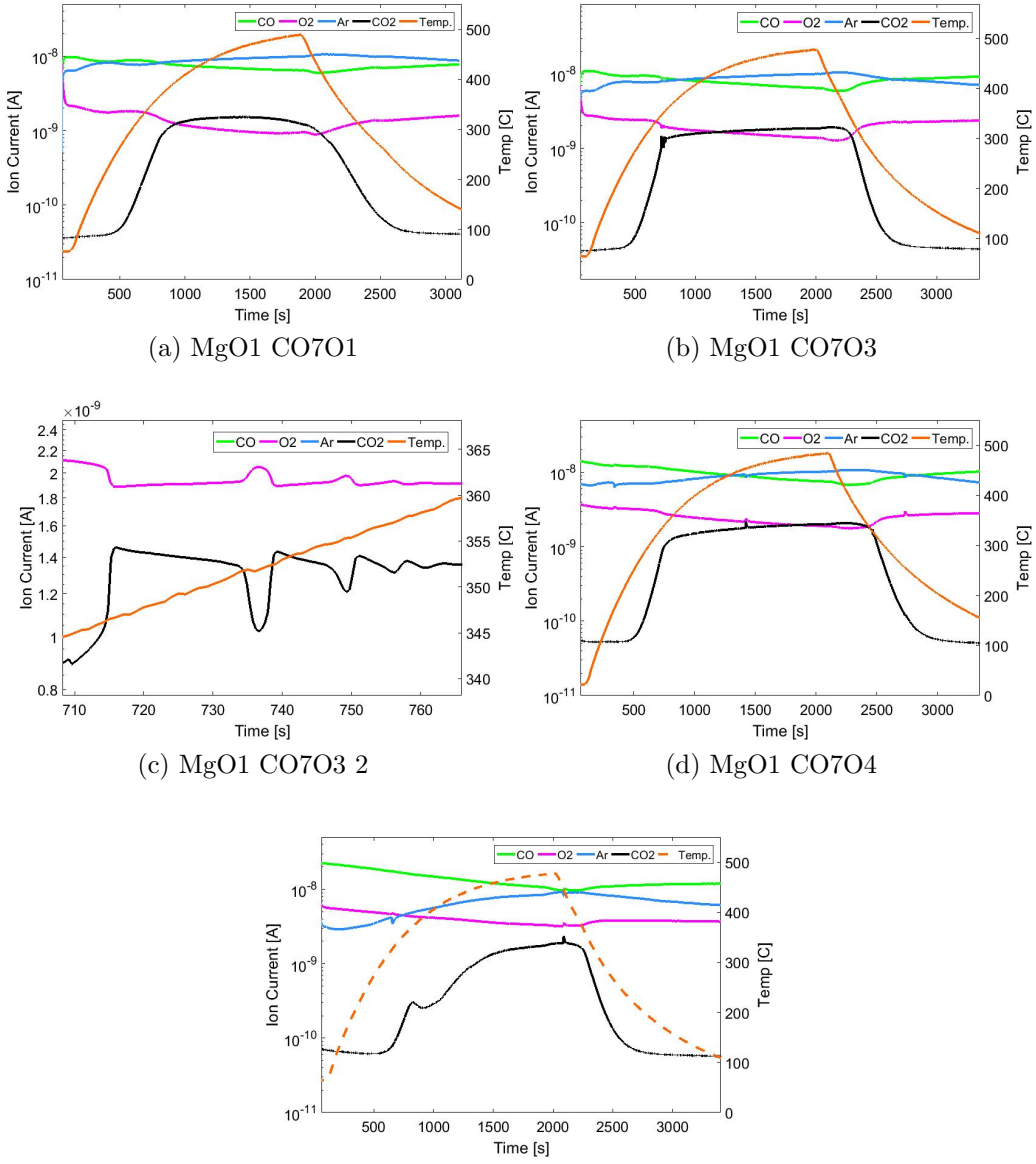

(a) MgO1 CO7O1

(b) MgO1 CO7O3

(c) MgO1 CO7O3 2

(d) MgO1 CO7O4

(e) MgO1 CO7O7

Figure 4.9: *Comprehensive CO oxidation mass spectra for MgO1. (a) is CO7O1, (b) is CO7O3, (c) is a close-up of the 670-820s section of (b). Finally, (d) and (e) are the complete CO7O4 and CO7O7 mass spectra.In the spectra: in orange the temperature, black line corresponding to* CO_2*. Ar is in light-blue, whether* O_2 *in magenta, concluding with CO in green. All the plots are presented as IonCurrent[A] and Temperature[°C] against Time[s]. Where Temp line is dashed the actual temperatures were not registered; since identical cycles were performed across all samples we reported a model Temp curve, reported from spectrum (d)*

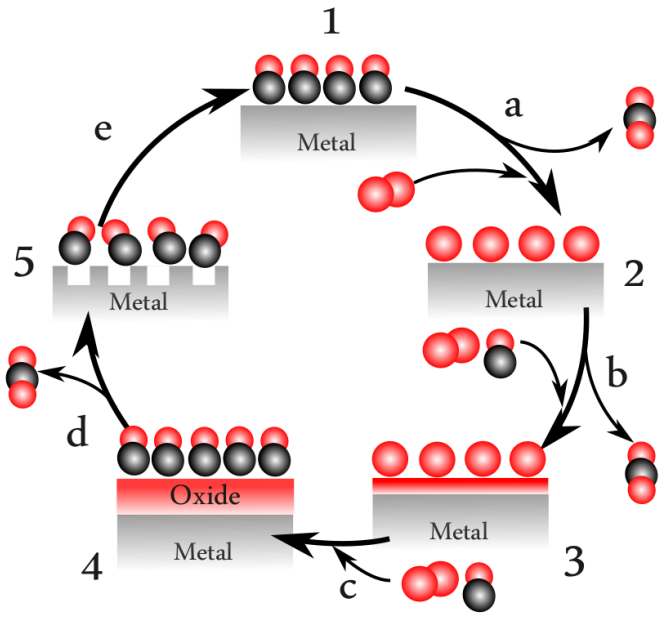

(a) Pd/Al_2O_3 catalytic Cycle

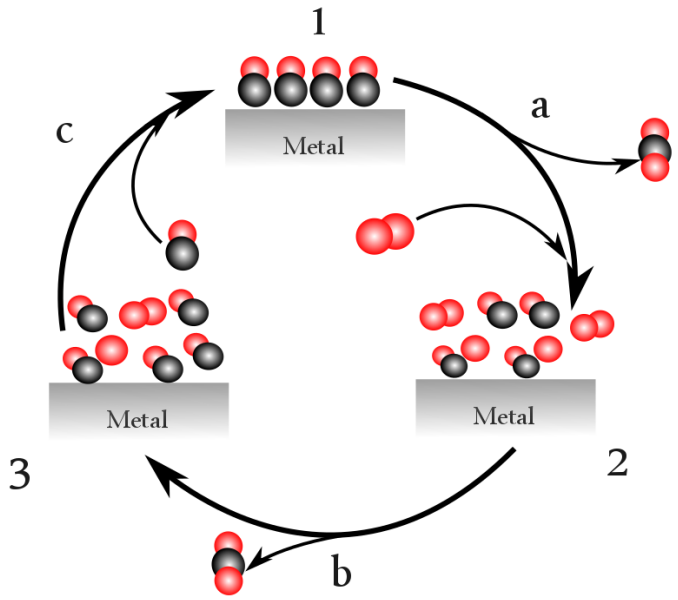

(b) Rh/MgO catalytic Cycle

Figure 4.10: *Pd/Al_2O_3 (a) and Rh/MgO (b) catalytic oscillation cycles. While in case (a) some of the literature support the illustrated mechanism [14] the cycle presented in (b) has not yet been reported*

cycle then continues until any of the experimental variables is changed.

It can be argued that this non-equilibrium catalytic-cycle, as for the one on Pd/Al_2O_3, occurs only in a narrow window T-P-Gas conditions: hence its metastable equilibrium during a steep temperature ramp, as during the CO7O3 experiment, it is very limited in time. In fact, it can be noted how, in the temperature interval considered, there is a drastic decrease in catalytic activity extrema for different temperatures: with maximum oscillation at around 355°C, and barely any oscillation at around 360°C. Finally, following the same argumentation, we can speculate on the presence of the oscillations in CO7O3 and not in CO7O4, whether they were present in two very different gas-compositions such as CO7O4 and CO7O7 for the Pd/Al_2O_3 sample. In fact, it can be noted how in the Pd case, since a rather substantial oxidation of the surface is present, the thermodynamic boundaries upon the T-P-Gas condition could be rather broad since its high-energy contribution. In the Rh case instead, and following our interpretation, only a weak balance between CO- and O_2- absorption energies generate the oscillations: tighten the T-P-Gas requirements of the system and destabilising the oscillations respect to a conventional behaviour.

Finally, for experiment CO7O7 shown in panel *(e)*, the light-off is covered by an interference in the catalysts system and unfortunately no precise measurement is available for this gas-ratio. Specifically, the spectrum in Fig. 4.9 *e*, is the very first thermal activation of the system after its preparation. The irregularity in the curve of CO_2 then can be explained as an interference phenomenon due to desorption and calcination of the sample that usually take place on its first heating. As interference then, it can be observed how this behaviour is absent in the subsequent reaction cycles.

Chapter 5

Conclusion

5.1 Substrate preparation-dependent particle growth

In this work we have prepared three samples, each one of which displays unique preparation-dependent characteristics.

MgO2 has been Ar^+ sputtered at 500 eV and O_2 annealed. These preparations have left a well ordered and clean surface of MgO(001) for the subsequent Rh deposition. The Rh has been deposited in what appears, from AFM ans SEM imaging, an homogeneous bed of NPs with diameters of ∼20nm and heights of ∼3nm. However, due to limitation in AFM imaging, and specifically limitation due to tip size, both measurements of diameter and coverage would need further investigations.

MgO3, prepared with similar parameters as MgO2, has undergone also a CeO_x reactive PVD by depositing $Ce_{(m)}$ on the heated sample in oxidizing atmosphere. This sample, both in AFM and SEM imaging, shows an identical morphology compared to the previous one, with the only noticeable difference being a lower tendency in charging effects when under SEM observation. Also MgO3 shows a nearly complete coverage of CeO_x/Rh with NPs of identical size compared to MgO2. No evident presence of CeO_x is acknowledged on the sample surface: further analysis seems appropriate to a deepen the knowledge of its morphology.

Finally, MgO1 which has undergone an harsh Ar^+ sputtering at 1,5 keV, presents a coexistence on its surface of a system of MPs and NPs. While the NPs have shown, via AFM, same dimensions compared to MgO2 and MgO3; the MPs have an average diameter of ∼1.5 μm and an average height of ∼50 nm. The coverage is similar to the one on the previous samples, with a partial coverage of 8% accounted from the MPs.

In this work we have obtained a good "recipe-procedure" to grow NPs with desired characteristics as a function the used substrate preparation. Moreover, we have tested and verified the experimental limitations of STM, AFM and SEM microscopies with respect to this type of sample, gaining better understanding for further developments.

5.2 Gas-composition dependent activity during CO oxidation

The CO oxidation has been tested with two different samples: MgO1 and a reference sample of powder catalyst which reference name Pd/Al_2O_3. Both of them were tested at four different gas ratios from highly O_2-rich to highly CO-rich, and with a complete temperature-cycle from room temperature to 500°C and from 500°C to room temperature, with a constant pressure of 800 mbar. This was done in order to check the reaction hyper-surface at different gas-composition points and for a complete range of temperatures.

The powder catalyst, in form of a pressed pellet, has shown for all the four gas mixtures a high catalytic activity and light-off temperatures from a minimum of 220°C for CO7O7 to a maximum of 320°C for CO7O1. Furthermore, an oscillatory behaviour in the catalytic activity was registered for the two O_2-rich compositions CO7O4 and CO7O7. This behaviour, already well documented in literature, has to be ascribed to the oxidation of the metal surface, where the oscillations are on their turn due to non-equilibrium phenomena near the catalyst surface; as shown in Fig. 4.10.

Sample MgO1, tested in the same conditions, has generally shown a lower catalytic activity compared to Pd/Al_2O_3, with a light-off at around 340-400°C, depending on the gas-ratio. Its activity also has also been found to be gas-mixture dependent as was the case for the test sample. Most interestingly though, it has shown an oscillatory behaviour in catalytic activity during the CO7O3 experiment. This kind of behaviour in CO-rich conditions has never been registered in literature before.

In this scenario, our proposed mechanism for this oscillatory behaviour, has to be accounted to a MTL regime due to a non-equilibrium distribution of the limiting reactant, oxygen, in the reactor environment. Beginning with a complete CO-covered surface at room temperature, at rising temperature a gradual dissociative absorption of O_2 from the surface begins. This, in turn, gradually leads to an increase in catalytic activity, until the complete light-off is reached, where all the O_2 absorbed is catalytically consumed. In a O_2-depleted environment though, as it is the one nearer to the catalyst

surface, it follows a new CO coverage of the surface, fostering in this way a new cycle.

Interesting new behaviours have been discovered from our Rh/MgO(001) samples during the oxidation cycles. After proposing a possible catalytic route for the observed behaviour, new measurements seem appropriate for a more thorough knowledge of the system. Furthermore, also a complete series of CO_2 hydrogenation tests have already been scheduled.

Chapter 6

Outlook

During the development of this work a number of interesting features have been unveiled that would be worth further investigations.

As seen in the Section 4.3 for what concern CO oxidation, the oscillations observed on sample MgO1 seems to have no precedent in literature: so that a more accurate and extensive series of experiments in similar conditions seems appropriate to further prove our mechanism hypothesis. Furthermore, testing at the same conditions also MgO2 and MgO3 could be useful to gain further insight and to verify possible influence of CeO_x on the reaction itself.

Also a series of tests concerning the CO_2 hydrogenation, since these kind of catalysts have shown important activity also on that reaction, are foreseen.

For what concern the microscopy side of the work, also a series of further AFM and SEM images for sintering effect investigation seems appropriate to complete the catalytic cycle determination on all the samples: from deposition, through reaction and post-processing analysis.

Finally, during SEM imaging as shown in Fig. 6.1, an interesting electrical behaviour from sample MgO2 has been reported: an intermittent "lightning pattern", from what seems to be a superficial discharging effect, appeared during analysis. Even if not strictly related to the topic of this work, and so not reported in the previous sections, the phenomenon seems to be not yet reported into literature, and so worth investigation for its potential future electronic applications

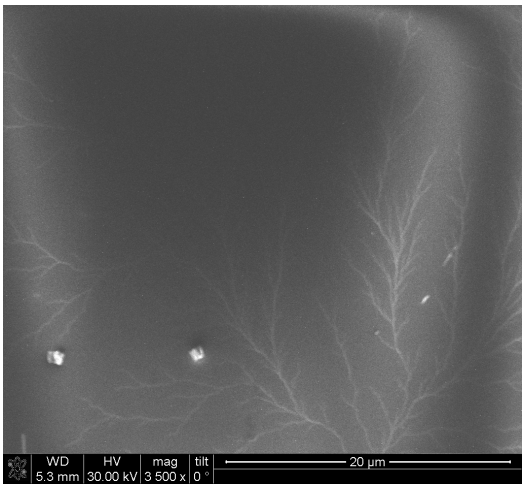

(a) Lightning pattern

Figure 6.1: *Lightning pattern (a) in SEM image on MgO2.*

6.1 Acknowledgements

I would like to immensely thank my supervisors, Uta Hejral and Johan Gustafson, for their time and help in bringing this thesis to its final stage. From the enlightening discussions to, and foremost, the endless time spent together doing measurements and reading this manuscript.

I would also like to thank all the people from Synchrotron Radiation Science Research, for their help and kindness. In particulal: Andreas Schaefer for providing his unique experience during preparation; Milena Moreira in her willingness to spend time and her expertise in SEM imaging and Jovana Colvin for her help in the AFM lab.

List of Figures

List of Tables

Bibliography

[1] Joel B. Smith. From global to regional climate change: Relative knowns and unknowns about global warming. *Fisheries*, 15(6):2–6, 1990.

[2] Gerald A. Meehl, Warren M. Washington, David J. Erickson, Bruce P. Briegleb, and Peter J. Jaumann. Climate change from increased co2 and direct and indirect effects of sulfate aerosols. *Geophysical Research Letters*, 23(25):3755–3758, 1996.

[3] K R Lawless. The oxidation of metals. *Reports on Progress in Physics*, 37(2):231, 1974.

[4] G.V. Mamontov, M.V. Grabchenko, V.I. Sobolev, V.I. Zaikovskii, and O.V. Vodyankina. Ethanol dehydrogenation over ag-ceo2/sio2 catalyst: Role of ag-ceo2 interface. *Applied Catalysis A: General*, 528:161 – 167, 2016.

[5] Anne Birot, Florence Epron, Claude Descorme, and Daniel Duprez. Ethanol steam reforming over rh/cexzr1xo2 catalysts: Impact of the co–co2–ch4 interconversion reactions on the {H2} production. *Applied Catalysis B: Environmental*, 79(1):17 – 25, 2008.

[6] Hitoshi Kusama, Kiyomi Okabe, Kazuhiro Sayama, and Hironori Arakawa. Co2 hydrogenation to ethanol over promoted rh/sio2 catalysts. *Catalysis Today*, 28(3):261 – 266, 1996.

[7] Bård Lindström and Lars J. Pettersson. A brief history of catalysis. *CATTECH*, 7(4):130–138, 2003.

[8] Gadi Rothenberg. *Catalysis: Concepts and Green Applications*. Wiley, 2010.

[9] Kurt W. Kolasinski. *Surface Science: Foundations of Catalysis and Nanoscience*. Wiley, 2012.

[10] Chorkendorff I. and Niemantsverdriet J.W. *Concept of modern catalysis and kinetics*. Wiley, 2003.

[11] Schlosser Manfred. *Organometallics in synthesis: a manual*. Wiley, 2013.

[12] Claude R. Henry. Morphology of supported nanoparticles. *Progress in Surface Science*, 80(3–4):92 – 116, 2005.

[13] Qiang Fu and Thomas Wagner. Interaction of nanostructured metal overlayers with oxide surfaces. *Surface Science Reports*, 62(11):431 – 498, 2007.

[14] Sara Blomberg, Jianfeng Zhou, Johan Gustafson, Johan Zetterberg, and Edvin Lundgren. 2d and 3d imaging of the gas phase close to an operating model catalyst by planar laser induced fluorescence. *Journal of Physics: Condensed Matter*, 28(45):453002, 2016.

[15] Antoine Beuls, Colas Swalus, Marc Jacquemin, George Heyen, Alejandro Karelovic, and Patricio Ruiz. Methanation of co2: Further insight into the mechanism over rh/-al2o3 catalyst. *Applied Catalysis B: Environmental*, 113–114:2 – 10, 2012. Natural Gas Conversion Symposium (NGCS 9) Special Issue.

[16] Daniel Duprez. Study of surface reaction mechanisms by 16o/18o and h/d isotopic exchange. *Catalysis Today*, 112(1–4):17 – 22, 2006.

[17] P. Nolte, A. Stierle, N. Y. Jin-Phillipp, N. Kasper, T. U. Schulli, and H. Dosch. Shape changes of supported rh nanoparticles during oxidation and reduction cycles. *Science*, 321(5896):1654–1658, 2008.

[18] Oliver Martin, Antonio J. Martín, Cecilia Mondelli, Sharon Mitchell, Takuya F. Segawa, Roland Hauert, Charlotte Drouilly, Daniel Curulla-Ferré, and Javier Pérez-Ramírez. Indium oxide as a superior catalyst for methanol synthesis by co2 hydrogenation. *Angewandte Chemie International Edition*, 55(21):6261–6265, 2016.

[19] Patrick Muller, Uta Hejral, Uta Rutt, and Andreas Stierle. In situ oxidation study of pd-rh nanoparticles on mgal2o4(001). *Phys. Chem. Chem. Phys.*, 16:13866–13874, 2014.

[20] D. Chester Upham, Alan R. Derk, Sudanshu Sharma, Horia Metiu, and Eric W. McFarland. Co2 methanation by ru-doped ceria: the role of the oxidation state of the surface. *Catal. Sci. Technol.*, 5:1783–1791, 2015.

[21] Hans-Joachim Freund, Gerard Meijer, Matthias Scheffler, Robert Schlögl, and Martin Wolf. Co oxidation as a prototypical reaction for heterogeneous processes. *Angewandte Chemie International Edition*, 50(43):10064–10094, 2011.

[22] Johan Nilsson, Per-Anders Carlsson, Sheedeh Fouladvand, Natalia M. Martin, Johan Gustafson, Mark A. Newton, Edvin Lundgren, Henrik Grönbeck, and Magnus Skoglundh. Chemistry of supported palladium nanoparticles during methane oxidation. *ACS Catalysis*, 5(4):2481–2489, 2015.

[23] Herjal Uta. Operando characterization of supported alloy nanoparticles during catalytic co oxidation by surface sensitive x-ray diffraction. *Department of Physics of Universität Hamburg*, 2015.

[24] Natalia M. Martin, Peter Velin, Magnus Skoglundh, Matthias Bauer, and Per-Anders Carlsson. Catalytic hydrogenation of co2 to methane over supported pd, rh and ni catalysts. *Catal. Sci. Technol.*, 7:1086–1094, 2017.

[25] Johan Gustafson et. al. Catalytic activity of the rh surface oxide: Co oxidation over rh(111) under realistic conditions. *Journal of Physical Chemistry C*, 114(10):4580–4583, 2010.

[26] David R. Mullins. The surface chemistry of cerium oxide. *Surface Science Reports*, 70(1):42 – 85, 2015.

[27] Paola Luches and Sergio Valeri. Structure, morphology and reducibility of epitaxial cerium oxide ultrathin films and nanostructures. *Materials*, 8(9):5818–5833, 2015.

[28] Tiziano Montini, Michele Melchionna, Matteo Monai, and Paolo Fornasiero. Fundamentals and catalytic applications of ceo2-based materials. *Chemical Reviews*, 116(10):5987–6041, 2016.

[29] Hans-Joachim Freund and Gianfranco Pacchioni. Oxide ultra-thin films on metals: new materials for the design of supported metal catalysts. *Chem. Soc. Rev.*, 37:2224–2242, 2008.

[30] Bas L. M. Hendriksen et. al. The role of steps in surface catalysis and reaction oscillations. *Nature CHemistry*, 2:730–734, 2010.

[31] Gustafson Johan. Oxidation of some late transition metal surfaces: Structural studies from uhv to atmospheric pressure. *Department of Synchrotron Radiation Research, Lund University*, 2006.

[32] J. Gustafson, R. Westerström, O. Balmes, A. Resta, R. van Rijn, X. Torrelles, C. T. Herbschleb, J. W. M. Frenken, and E. Lundgren. Catalytic activity of the rh surface oxide: Co oxidation over rh(111) under realistic conditions. *The Journal of Physical Chemistry C*, 114(10):4580–4583, 2010.

[33] S. Hofmannr. *Auger and X-Ray Photoelectron Spectroscopy in Material Science: a User-Oriented Guide*. Springer, 2013.

[34] L. E. Davis. *Handbook of Auger Electron Spectroscopy, Second Edition*. Physical Electronic Division, Perkin-Elmer Corporation, 1976.

[35] C.J. Powell. *NIST Electron Inelastic Mean-Free-Path Database*, 1.2 edition, 2010.

[36] P. Hofmann. *Solid State Physics: an introduction*. Wiley, 2015.

[37] Hagman Benjamin. Structure and reactivity of surface oxides on cu(100). *Division of Synchrotron Radiation Research, Physics Department, Lund University*, 2017.

[38] Bert Voigtlaender. *Scanning Probe Microscopy: Atomic Force Microscopy and Scanning Tunneling Microscopy*. Springer, 2015.

[39] Davide Ricci and P.C. Braga. *Atomic Force Microscopy: Biomedical Methods and Applications*, volume 242 of *Methods in Molecular Biology*. Humana Press, 2003.

[40] Y. Lykhach, T. Staudt, R. Streber, M. P.A. Lorenz, A. Bayer, H.-P. Steinrück, and J." Libuda. Co2 activation on single crystal based ceria and magnesia/ceria model catalysts. *The European Physical Journal B*, 75(1):89–100, 2010.

[41] F. Dvořák, O. Stetsovych, M. Steger, E. Cherradi, I. Matolínová, N. Tsud, M. Škoda, T. Skála, J. Mysliveček, and V. Matolín. Adjusting morphology and surface reduction of ceo2(111) thin films on cu(111). *The Journal of Physical Chemistry C*, 115(15):7496–7503, 2011.